2005

Effects of sediment iron mineral composition on microbially mediated changes in divalent metal speciation: Importance of ferrihydrite

D. Craig Cooper
Idaho National Laboratory, craig.cooper@inl.gov

Andrew L. Neal
University of Georgia

Ravi K. Kukkadapu
Pacific Northwest National Laboratory, ravi.kukkadapu@pnl.gov

Dale Brewe
Argonne National Laboratory

Aaron Coby
Indiana University

See next page for additional authors

Geochimica et Cosmochimica Acta, Vol. 69, No. 7, pp. 1739–1754, 2005

0016-7037/05 $30.00 + .00

ELSEVIER

doi:10.1016/j.gca.2004.09.013

Effects of sediment iron mineral composition on microbially mediated changes in divalent metal speciation: Importance of ferrihydrite

D. Craig Cooper,[1,*] Andrew L. Neal,[2] Ravi K. Kukkadapu,[3] Dale Brewe,[4] Aaron Coby,[5] and Flynn W. Picardal[5]

[1]Geosciences Research, Idaho National Laboratory, P.O. Box 1625, MS 2107, Idaho Falls, ID 83415-2107, USA
[2]Savannah River Ecology Laboratory, University of Georgia, Drawer E, Aiken, SC 29802, USA
[3]Environmental Molecular Science Laboratory, P.O. Box 999, MS K8-96, Richland, WA 99352, USA
[4]Argonne National Laboratory, Bldg. 435E Sector 20, 9700 S. Cass Ave., Argonne, IL 60439, USA
[5]School of Public and Environmental Affairs, Indiana University, 1315 E. 10th St., Bloomington, IN 47405, USA

(*Received February* 10, 2004; *accepted in revised form September* 10, 2004)

Abstract—Dissimilatory metal reducing bacteria (DMRB) can influence geochemical processes that affect the speciation and mobility of metallic contaminants within natural environments. Most investigations into the effect of DMRB on sediment geochemistry utilize various synthetic oxides as the Fe^{III} source (e.g., ferrihydrite, goethite, hematite). These synthetic materials do not represent the mineralogical composition of natural systems, and do not account for the effect of sediment mineral composition on microbially mediated processes. Our experiments with a DMRB (*Shewanella putrefaciens* 200) and a divalent metal (Zn^{II}) indicate that, while complexity in sediment mineral composition may not strongly impact the degree of "microbial iron reducibility," it does alter the geochemical consequences of such microbial activity. The ferrihydrite and clay mineral content are key factors. Microbial reduction of a synthetic blend of goethite and ferrihydrite (VHSA-G) carrying previously adsorbed Zn^{II} increased both [Zn^{II}-aq] and the proportion of adsorbed Zn^{II} that is insoluble in 0.5 M HCl. Microbial reduction of Fe^{III} in similarly treated iron-bearing clayey sediment (Fe-K-Q) and hematite sand, which contained minimal amounts of ferrihydrite, had no similar effect. Addition of ferrihydrite increased the effect of microbial Fe^{III} reduction on Zn^{II} association with a 0.5 M HCl insoluble phase in all sediment treatments, but the effect was inconsequential in the Fe-K-Q. Zinc *k*-edge X-ray absorption spectroscopy (XAS) data indicate that microbial Fe^{III} reduction altered Zn^{II} bonding in fundamentally different ways for VHSA-G and Fe-K-Q. In VHSA-G, ZnO_6 octahedra were present in both sterile and reduced samples; with a slightly increased average Zn-O coordination number and a slightly higher degree of long-range order in the reduced sample. This result may be consistent with enhanced Zn^{II} substitution within goethite in the microbially reduced sample, though these data do not show the large increase in the degree of Zn-O-metal interactions expected to accompany this change. In Fe-K-Q, microbial Fe^{III} reduction transforms Zn-O polyhedra from octahedral to tetrahedral coordination and leads to the formation of a $ZnCl_2$ moiety and an increased degree of multiple scattering. This study indicates that, while many sedimentary iron minerals are easily reduced by DMRB, the effects of microbial Fe^{III} reduction on trace metal geochemistry are dependent on sediment mineral composition. *Copyright © 2005 Elsevier Ltd*

1. INTRODUCTION

Dissimilatory reduction of iron oxide minerals has been documented for a large number of microorganisms in a wide range of environments (Lovley, 1997), and has become recognized as an important constituent of the global carbon and iron cycles (Lovley, 1987, 1991, 1997; Konhauser, 1998). This process has a profound effect on groundwater and sediment geochemistry and can significantly alter the speciation and mobility of contaminant metals. Many investigations into this phenomenon have examined the ability of dissimilatory metal reducing bacteria (DMRB) to reduce various crystalline Fe^{III} sources (e.g., Roden and Zachara, 1996; Zachara et al., 1998; Bousserrhine et al., 1999; Kostka et al., 2002; Lee et al., 2002; Dong et al., 2003). The impact of DMRB activity on sediment mineral composition and metal geochemistry has also been extensively researched (e.g., Lovley, 1993; Fendorf et al., 2000; Fredrickson et al., 2000, 2001, 2002; Wielinga et al., 2000; Zachara et al., 2001; Lloyd et al., 2002). Most of these laboratory investigations utilize either "standard" or synthetic minerals that artificially constrain the experimental systems and do not reflect the complex mineral composition of natural environments. Thus, there are scant data to allow proper linkage between laboratory experimentation and field observation. Therefore, we examined the effect(s) of complex sediment composition on the geochemical outcome of microbial Fe^{III} reduction.

Previous research indicates that differences in sediment iron speciation can control the effect of microbial iron reduction on iron speciation and metal geochemistry. Zachara et al. (1998) report that iron oxide minerals in natural sediments are more "microbially reducible" than their synthetic counterparts, and that the presence of nonreducible phases does not inhibit microbial Fe^{III} reduction. Kukkadapu et al. (2001) have shown that the presence of nonreducible phases does not inhibit microbial Fe^{III} reduction in natural sediments and noted that adsorption of Fe^{II} to these nonreducible phases inhibits the overall degree of iron biomineralization. With respect to metals, Zachara et al. (2000) report that Fe^{II} adsorption to natural sediments can alter the dynamics of how Fe^{II} and a transition

* Author to whom correspondence should be addressed (craig.cooper@inl.gov).

metal (Co^{II}) reacts with an organic ligand in an Fe^{III} reducing environment.

Microbial reduction of iron oxides has been considered as a strategy for remediating metal and radionuclide contamination in sediments. In some cases, remediation may result from direct changes in the contaminant's redox state, resulting in altered mobility or toxicity. In other cases, microbial reduction of ferric iron and/or humic material may cause complex changes in system geochemistry that can result in precipitation/dissolution reactions, altered oxide crystallinity, and/or changes in the mobility of adsorbed contaminants. For example, Cooper et al. (2000) report that microbial reduction of goethite (α-FeOOH) did not have the same geochemical effect on the speciation of an adsorbed metal ion as microbial reduction of lepidocrocite (γ-FeOOH). Both goethite and lepidocrocite were reduced to similar degrees at equivalent rates, yet lepidocrocite reduction incorporated previously adsorbed Zn^{II} into biogenic magnetite while goethite reduction did not. Thus, sediment iron geochemistry can provide an important control on the products of microbial iron reduction and the geochemistry of metallic contaminants in certain environments.

In contrast, most studies of the effect of sediment iron geochemistry on the degree of "microbial reducibility" conclude that reactive surface area of sediment iron minerals is generally considered to be more important to DMRB than the minerals' crystal structure. Roden and Zachara (1996) report that the rate and extent of microbial reduction of synthetic iron oxide minerals correlated with iron oxide surface area rather than the calculated free energy (ΔG_{rxn}) for the system. Zachara et al. (1998) also observed this surface area effect for geologic iron oxides, and hypothesized that microheterogeneities in the iron oxide crystal structure may increase the reactive surface area of the iron-bearing mineral phases. Rosso et al. (2003) observed the importance of such microheterogeneities, and used observations of preferential Fe^{III} reduction in heterogeneous regions to demonstrate that *S. putrefaciens* CN32 can reduce crystalline Fe^{III} via a metabolic strategy that utilizes nonlocal electron transport. Previous studies also indicate that microbial utilization of electron shuttling compounds can help DMRB to overcome energy barriers associated with trace metal substitution in iron oxide minerals (Fredrickson et al., 2001), and enhance the efficacy of iron complexing ligands (Royer et al., 2002). Thus, it is important to distinguish between the processes by which a microorganism (or microbial community) induces a perturbation, such as Fe^{III} reduction, within a system and the way in which the system responds to that perturbation.

This study seeks to identify how variable iron oxide composition in a sediment system can affect the way(s) that system responds to a microbial perturbation (dissimilatory Fe^{III} reduction), and how such a response may affect the speciation of divalent metals. Zn^{II} was chosen because it is a divalent metal that; (i) is not sensitive to redox changes, (ii) has an ionic diameter similar to that of iron, (iii) is relatively soluble at pH ~7, (iv) does not form strong aqueous complexes in "typical" groundwater, and (v) has well defined adsorption chemistry with a variety of mineral surfaces. In addition, Zn^{II} has a cation exchange selectivity coefficient similar to that of Ca^{II} and forms a number of carbonate minerals at elevated carbonate alkalinity and circumneutral pH (Stumm and Morgan, 1981; Appelo and Potsma, 1996). Goethite was chosen as a synthetic sediment to allow comparison with our previous work that examined the effect of microbial goethite reduction on Zn^{II} geochemistry (Cooper et al., 2000). A small number of experiments were conducted with synthetic hematite to enable better comparison between experiments with synthetic goethite and the selected natural sediments. Natural sediments were chosen to encompass the suite of physical properties and iron-bearing minerals that are commonly found in natural systems. We chose to employ natural sediments with clay mineral composition dominated by kaolinite, since microbial reduction of structural Fe^{III} in smectite and illite clays can alter clay mineral morphology and/or surface chemical properties (e.g., Gates et al., 1998; Gates et al., 1996; Kostka et al., 1999; Dong et al., 2003). The selected sediments also contained low levels of 0.5 M HCl soluble iron, thereby allowing us to specifically test the importance of ferrihydrite content through experiments with mixtures of natural sediments and synthetic ferrihydrite.

2. MATERIALS AND METHODS

2.1. Microorganism and Culture Conditions

Shewanella putrefaciens is a gram-negative, motile rod with an obligate respiratory metabolism (Semple and Westlake, 1987). The strain used in these experiments, *S. putrefaciens* 200, was originally isolated by Obuekwe (1980) from a Canadian oil pipeline. The culture was maintained on solid media of nutrient agar containing 5 g L^{-1} yeast extract (Difco, Detroit, MI, USA) as previously described (Picardal et al., 1993). Cultures were grown as suspensions in a 2.5-L Bioflow 3000 Fermentor (New Brunswick Scientific Co., Edison, NJ, USA) in a liquid medium that consisted (per liter) of 2.0 g Na_2SO_4, 0.5 g K_2HPO_4, 1.0 g NH_4Cl, 0.198 g $CaCl_2 \cdot 2H_2O$, 0.1 g $MgSO_4 \cdot 7H_2O$, 19.35 mg $FeCl_3 \cdot 6H_2O$, 0.5 g yeast extract, and 3 mL of 60% (w/v) sodium lactate. Following an initial period of aerobic growth, anaerobic reductase activity was induced by reducing the air-flow to ~100 mL min^{-1} and maintaining the cells under suboxic ($[O_2]_{(aq)} < 2.5$ μmol L^{-1}) conditions for 12 h. *S. putrefaciens* cells were harvested by centrifugation and resuspended to a target optical density (A_{600} = ~1.2) in artificial groundwater (AGW) medium. Small aliquots of this cell concentrate were subsequently used to inoculate the experimental slurries. The *Geobacter sulfurreducens* (Caccavo et al., 1994) used in some experiments was kindly provided by Dr. Derek Lovley (University of Massachusetts), and was utilized to determine if results were specific to *S. putrefaciens* or might be more generally applied to the process of microbial iron reduction. *G. sulfurreducens* was grown under anaerobic conditions in 500-mL serum bottles using the AGW previously described (Cooper et al., 2000) which had been modified by replacing sulfate salts with the respective chloride salts. Fumarate and acetate were utilized respectively as the electron acceptor and donor for growth. After several days of growth, cells were removed by centrifugation and resuspended under anaerobic conditions in deoxygenated AGW medium to yield the inoculum used in experiments.

2.2. Iron Reduction Experiments with Zn^{II} and Various Solid-Phase Fe^{III} Substrates

The anaerobic AGW used in these experiments has been described previously (Cooper et al., 2000), and consists of a minimal salts medium with added lactate and 10 mM HEPES (organic pH buffer). The ferrihydrite and synthetic goethite samples of varying surface area were prepared as described by Schwertmann and Cornell (1991). Sediments MNC-71 (referred to as Fe-K-Q) and EHS (Eatonton Hematite Sand, referred to as H-sand) were obtained from the Department of Energy (DOE) subsurface collection in 1998. This collection is now managed by the DOE-NABIR (Natural and Accelerated BioRemediation) program's Field Research Center at Oak Ridge National Laboratory, and these particular sediments are no longer widely available. H-sand was collected from Atlantic Coastal Plain sediments in Eatontown, NJ; and its mineral composition has been previously described

(Zachara et al., 1998). Fe-K-Q was collected from iron-bearing, clayey sediments at Marshall, NC, and we are not aware of any previous reports investigating its mineral content. Synthetic hematite was purchased from J.T. Baker/Mallinckrodt Baker Inc. (Phillipsburg, NJ). The artificial groundwater (AGW) medium used in these experiments also contained 10 mmol L^{-1} HEPES buffer (99.5% as Na-salt, CAS# = 75277-39-3, N-[2 Hydroxyethyl]piperazine-N′-[2-ethanesulfonicacid]) and 10 mmol L^{-1} lactate as an electron donor. Anaerobic Zn^{II} stock solution was prepared by dissolving $ZnCl_2$*$2H_2O$ in Milli-Q water and adjusting to pH 6.0 with 10.0 M NaOH. Stock solution was sterilized by autoclaving and an aliquot was subsequently added to the AGW media so that the concentration of total added Zn^{II} was 225 μmol L^{-1}. H-sand and Fe-K-Q were initially sterilized by Tyndallization (sequential autoclaving), and were autoclaved (dry) again immediately before individual experiments. Sediments were not washed or otherwise modified before experimentation. A small mass of the solid used in each set of experiments was set aside for X-ray diffraction (XRD) and surface area analyses. For the experimental slurry, enough sediment to account for 1 mmol of citrate-dithionite-bicarbonate (DCB) extractable iron in bulk sediment (Mehra and Jackson, 1960) was added to a set of acid-washed, anaerobic culture (Balch) tubes (Bellco, 25 mL nominal volume). The amount of sediment needed to account for 1 mmol DCB-iron was ~0.09 g of goethite, 0.16 g hematite, 1.3 g Fe-K-Q, 1.6 g H-sand per tube. For experiments with ferrihydrite additions, the total amount of DCB-Fe was held constant and the relative proportions of sediment DCB-Fe and ferrihydrite DCB-Fe were varied. Tubes containing dry oxide or sediment were autoclaved and cooled in an anaerobic chamber (Coy Laboratory Products) containing 95%–98%N_2 and 2%–5%H_2. Using sterile techniques, 20 mL sterile AGW medium amended with lactate, HEPES, and Zn^{II} was added to the tubes under anaerobic conditions. Tubes were crimp sealed with acid-washed butyl rubber stoppers and equilibrated on a shaker table (horizontal orientation) for 7 d before inoculation. Initial bottle headspace in all cases was ~95%N_2 with 5%H_2, and sediment in the tubes was manually resuspended once per day. Experiments with added ferrihydrite were conducted similarly except that sterile ferrihydrite was added as a Pasteurized slurry rather than as an autoclaved powder.

Before inoculation with *S. putrefaciens*, an initial set of samples (t_0) was collected. Due to the difficulty in obtaining repeatable aliquots of coarse-grained sediments from suspended slurries, sets of 5 Balch tubes (3 inoculated and 2 uninoculated) were sacrificed at each sampling interval. Each set of 5 Balch tubes contained one sediment type. Reported values are the average and standard deviation of analyses conducted on tubes sampled at the same time. Fe^{III} reduction experiments were initiated by inoculating slurries with 0.5 mL of *S. putrefaciens* suspension under anaerobic conditions. This dilution resulted in an estimated initial culture optical density (A_{600}) of 0.020, corresponding to ~2×10^6 cells mL^{-1}. At each periodic sampling point, a set of Balch tubes were removed from the shaker table, manually inverted to enhance slurry mixing, and then centrifuged (30 min, 4000 *g*) to separate liquid from solid. Supernatants were clear and no visible signs of colloidal suspensions were noted in the aqueous phase. The centrifuged tubes were than transferred to the anaerobic chamber, opened, and sampled for pH, aqueous Fe^{II}, and aqueous Zn^{II}. Aqueous Fe^{II} was analyzed immediately via a modified version of the ferrozine technique (Stookey, 1970; Kostka and Luther, 1994), and aqueous Zn^{II} was acidified and stored for later analysis. This modification generally involves adding an aliquot of the analyte solution into an excess ferrozine reagent solution (10 mM HEPES, 1 g/L ferrozine), and waiting ~15 min for color to fully evolve. The remaining supernatant was discarded, the sediments were resuspended in 20 mL of 0.5 M HCl, the tubes resealed inside the anaerobic chamber, and then transferred to a rotary mixer where they were digested for 2 h at room temperature. Tubes were then centrifuged (30 min, 4000 *g*) and the supernatant sampled for Fe^{II} and Zn^{II}. This "bound" fraction represents the solid fraction that is soluble in 0.5 N HCl. The reader is cautioned that "bound" is distinct from the terms Fe^{II}-sum and Zn^{II}-sum, which refer to the *sum* of "aqueous" and "bound" Fe^{II} and/or Zn^{II}. "Bound" Fe^{II} was analyzed immediately via the ferrozine technique, and "bound" Zn^{II} was stored for subsequent analysis. The remaining supernatant was decanted and the solid pellet was resuspended in 6.0 M HCl and digested for 72 hrs. Tubes were centrifuged (30 min, 4000 *g*) again and the supernatant was sampled for "strongly bound" Zn^{II} (strongly bound = solid fraction not soluble in 0.5 M HCl). Data for "strongly bound" Fe^{II} are not presented, as the strong acid also dissolves a large amount of Fe^{III}, which interferes with the ferrozine analysis. Previous studies into the potential for producing "strongly bound" Fe^{II} during microbial goethite reduction (Cooper et al., 2000) have determined that this fraction constitutes less than ~10% of total Fe^{II} under these conditions. Total Zn^{II} was defined as the sum of "aqueous," "bound," and "strongly bound," and acidified samples of supernatant for Zn analysis were stored in acid-washed polyethylene bottles for subsequent analysis via flame atomic adsorption spectrophotometry (AAS). The sequence of 0.5 M HCl followed by 6.0 M HCl extractions for concomitant quantification of Fe^{II} and Zn^{II} fractions was chosen over other combinations (e.g., acid oxalate, citrate dithionite) for several reasons. The chemical reagents used to prepare oxalate and dithionite solutions often contain small amounts of Zn^{II} that can contaminate samples and reduce precision. Prior studies suggest that a 2.0 h 0.5 M HCl extraction may be more selective for ferrihydrite than alternate approaches (Kostka and Luther, 1994). We wanted to be able to contrast these results with prior work investigating the effects of microbial iron mineral reduction on Zn^{II} adsorption chemistry (Cooper et al., 2000).

2.3. Wet Chemical Analyses and Sediment Characterization

Surface area was measured by 5-point BET N_2 adsorption in a Micromeritics Gemini 2360 surface area analyzer, after 2 h degassing under N_2 atmosphere at 120°C in a Micromeritics Flowprep 060. Grain size distribution was determined by sieving aliquots of whole sediment, and the iron content of bulk sediment and sediment size fractions was determined by wet chemical extraction with subsequent Fe analysis by flame AAS. Iron content was also determined via citrate dithionite (DCB) extractions (Mehra and Jackson, 1960). Cation exchange capacity was determined by the method of Amrhein and Suarez (1990), which calculates CEC as the sum of displaced ions while accounting for calcite and gypsum dissolution. Solution pH was measured inside the anaerobic chamber with a Cole Parmer gel-filled, epoxy combination electrode calibrated with pH 4 and pH 7 standard NBS buffers. The concentration of Zn^{II} in acidified extracts was determined by flame AAS using a Perkin Elmer 4100 flame atomic absorption spectrophotometer. For colorimetric analysis of ferrozine-treated Fe^{II} samples, the absorbance at 562 nm was measured on a Schimadzu UV-2101PC UV/VIS spectrophotometer. Metal standards for AAS analysis were prepared by diluting aliquots of certified commercial standards in 0.5 M HCl, and Fe^{II} standards were diluted from a concentrated stock solution of ferrous sulfate in 0.5 M HCl. Unless otherwise noted, all solutions were prepared using Milli-Q water (R = 18 MΩ). All experiments, extractions, and analyses were performed in acid-washed glassware and plasticware, and procedural blanks consisting of Milli-Q water were sampled regularly to monitor for potential metal contamination.

Samples for X-ray diffraction (XRD) analysis were prepared by two different methods. Dry samples of goethite, hematite, H-sand, and Fe-K-Q were ground in a ball mill to a fine powder, sieved through a U.S. Standard 200 mesh (less than ~ 75 μm dia.), and then prepared for XRD analysis via standard powder techniques. Because milling exposes samples to atmospheric gasses and will result in oxidation of ferrous moieties, numerous XRD analyses were also performed on specially prepared filter cakes. These samples were prepared by placing a rubber O-ring onto a 0.45 μm glass fibre filter of similar diameter. While under an oxygen-free atmosphere (95% N_2: 5% H_2) ~ 2 mL aliquots of slurry solution were pipetted onto the filter and the water allowed to drain through the filter. This process was repeated 3–5 times, until a ~1 mm thick cake was built up upon the filter. The filter cakes were dried over Drierite for 48 h in the anaerobic chamber, and then the glass fiber filter was transferred onto a glass slide and coated with cellulose acetate to minimize oxidation of ferrous moieties. This technique raises the sediment from the surface of the slide and produces an offset in the correlation between 2-*theta* and intensity. Since the dry-powder samples revealed that H-sand and Fe-K-Q contained a large amount of quartz, the "filter-cake" diffractograms for these sediments were corrected to the quartz peak at 2-*theta* = 26.5. Similarly prepared samples of VHSA-G were corrected to the goethite peak at 2-*theta* = 37. This technique has been employed successfully for preserving samples for XRD analysis of fine-grained microbially reduced goethite and lepidocrocite (Cooper et al., 2000). XRD diffrac-

Table 1. Summary of important geochemical properties of primary sediments used in these experiments

	VHSA goethite	Fe-kaolinite-quartz	Hematite sand
BET surface area (m^2/g)	95	38.4	2.1
0.5 M HCl extractable Fe (mg/g whole sediment)	47	0.5	0.1
Citrate dithionite extractable (DCB) Fe (mg/g whole sediment)	629[a]	44	25–40
Sediment mass% <150 μm	100%	42%	1–3%
Sediment mass % 150–300 μm	0	22%	6–8%
Sediment mass % 300–600 μm	0	30%	27%
Sediment mass % 600–850 μm	0	5%	13%
Sediment mass % 850 μm–2.0 mm	0	1%	51%
DCB Fe <150 μm[c] (percent of total Fe)	100%	43%	76–88%[b]
DCB Fe 150–300 μm	0	20%	6–12%
DCB Fe 300–600 μm	0	19%	3–7%
DCB Fe 600–850 μm	0	18%	2–3%
DCB Fe 850 μm–2.0 mm	0	<0.1%	1–2%

[a] Calculated from molar mass, assuming the chemical composition of VHSA goethite is FeOOH.
[b] Calculated by difference, and subject to error due to small mass of this fraction.
[c] DCB refers to the citrate dithionite extractable fraction.

tograms for microbially reduced sediments were generated on a Phillips XRG 3100 with a Cu K_α source, with a step size of 0.03 and a count time of 1–2 s. These conditions requires ~2 h to conduct a full scan, and prior experiments (Cooper et al., 2000) indicate that these conditions protect the filter cake from oxidation while providing reasonably precise diffractograms. A step size of 0.02 and a count time of 4 s was used for nonreduced sediments.

2.4. Mössbauer and X-ray Absorption Spectroscopy

For Mössbauer spectroscopy, randomly oriented absorbers (samples) were prepared by mixing ~30–40 mg of VHSA-G or ~100 mg Fe-K-Q sample with petroleum jelly in a 0.375-in. thick and 0.5-in. ID Cu holder sealed at one end with clear scotch tape. The holder was entirely filled with petroleum jelly/sample and then sealed at the other end with scotch tape. In addition to the scotch tape, an oxygen impermeable polymer film (aluminized-Mylar) was added as an outer seal on the both ends of the holder. Both the tape and polymer were snapped into the holder at the ends with rings made of carbonized-polyethyletherketone (PEEK) polymer to ensure tightness. Spectra were collected using a 50 mCi (initial strength) ^{57}Co/Rh single-line thin source. The Mössbauer bench (MB-500; WissEl, Germany) was equipped with a dual Mössbauer drive system to gather data simultaneously for two experiments. The velocity transducer MVT-1000 (WissEL) was operated in constant acceleration mode (23 Hz, ±10 mm s^{-1}). An Ar-Kr energy-proportional counter was used to detect the radiation transmitted through the holder, and the counts were stored as a function of energy (transducer velocity) using a 1024-channel analyzer. Data were folded to 512 channels to give a flat background and a zero-velocity position corresponding to the center shift (CS or δ) of a metallic iron foil at room temperature (RT). Calibration spectra were obtained with a 20-μm-thick α-Fe(m) foil (Amersham, United Kingdom) placed in exactly the same position as the samples to minimize any errors due to changes in geometry. A top-loading Janis exchange-gas cryostat was used to cool the sample to liquid nitrogen temperature (77K). For the 77-K measurements, both the source and drive assembly were held at room temperature. All Mössbauer spectra (RT and 77 K) were fitted with quadrupole splitting (QSDs) and/or hyperfine splitting distributions (HFDs) using the Voigt-based fitting method of Rancourt and Ping (Rancourt and Ping, 1991), using the *Recoil* program (University of Ottawa, Canada), and sample-thickness corrections were not carried out.

Fluorescence yield Zn *k*-edge X-ray absorption spectroscopy (XAS) measurements were collected on undulator beamline ID20 operated by the Pacific Northwest Consortium Collaborative Access Team (PNC-CAT) at the Advanced Photon Source, Argonne National Laboratory. Measurements were made at room temperature on sediment samples removed from Balch tubes and prepared under an anaerobic atmosphere. The samples were mounted in a custom poly(styrene) sample holder, sealed with X-ray translucent Kapton windows and flushed continuously with an H_2/He gas mixture. A Si(111) double crystal monochromator was used to select X-ray energies for step scans through the Zn *k* edge, and detuned by ~30% to reduce harmonics. An ionization chamber was used to monitor the incident x-rays and a 13 element Ge solid-state detector was used to collect the Zn fluorescence. Aluminum and copper filters were placed in front of the 13 element Ge detector to reduce the background due to Fe fluorescence and elastically and Compton-scattered X-rays, respectively. Data were collected across the Zn *k*-edge region at a step size of 0.8 eV. In the EXAFS region the absorption step size was 0.05 $Å^{-1}$ Data analysis was performed with *Athena* and *Artemis* in the *IFEFFIT* software package (Newville, 2001). Standard techniques were used to normalize the absorption spectra to the edge jump, and the *Autobk* algorithm was used to extract the EXAFS oscillations from the smoothed background. This algorithm produces excellent background subtraction to energies near the adsorption edge (Newville et al., 1993). Fitting of the near-neighbor coordination shell was performed in *R*-space after Fourier-Transforming the EXAFS with k^3 weighting over a range from 0.5 to 9 $Å^{-1}$ with a 2 $Å^{-1}$ Kaiser-Bessel weighting. Theoretical standards used in the fitting procedures and EXAFS background subtraction were generated by *FEFF7* (Zabinsky et al., 1995; Ankudinov and Rehr, 1997).

3. RESULTS

3.1. Characterization of Goethite and Sediments

Summary results from sediment characterization work for the primary sediments used in these experiments are presented in Table 1. VHSA goethite (VHSA-G) is a fine-grained synthetic goethite with a high surface area (95 m^2 g^{-1}) and all particles have a diameter <150 μm. Since the oxide was not acid-washed to remove low crystallinity precipitates, the VHSA-G may also contain small amounts of ferrihydrite. Fe-kaolinite-quartz (Fe-K-Q) is a clayey sand with a moderate surface area (38 m^2 g^{-1}), and a cation exchange capacity of ~12 ± 5 mEq 100 g^{-1}. This sediment contains ~4%–5% citrate dithionite (DCB) extractable iron by mass, with most of the Fe-K-Q mass and DCB-extractable iron found in the smaller grain size fractions. Hematite-sand (H-sand) is hematite-coated sand with a low surface area (2 m^2 g^{-1}), containing ~2.5–4.0% DCB-extractable iron by mass. The major portion of the sediment mass is found in the larger grain size fractions, but most of the DCB-extractable iron is found in the smallest grain size fractions. H-sand also contains a small amount of

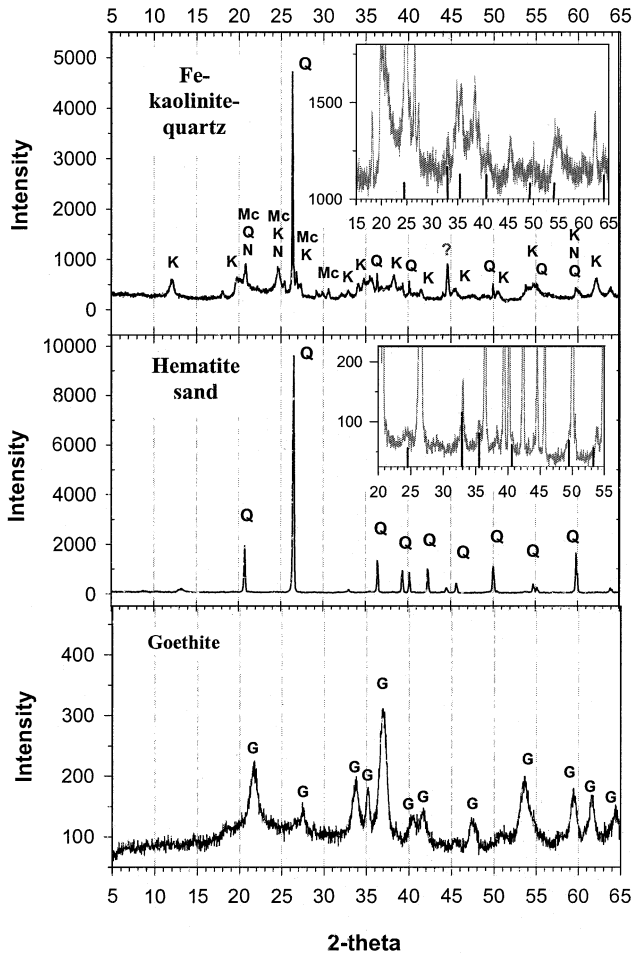

Fig. 1. Powder XRD diffractograms for VHSA goethite (VHSA-G), hematite-sand (H-sand), and Fe-kaolinite-quarts (Fe-K-Q). Inset for H-sand and Fe-K-Q zoom in on the minor phases and have same axes as overall plot. Lines in inset plots mark six major peaks for hematite. Peaks for kaolinite (K), neotocite (N), quartz (Q), microcline (Mc), and unidentified phase (?) are also marked in the diffractograms for H-sand and Fe-K-Q.

kaolinite (Zachara et al., 1998). The 0.5 M HCl extractable iron, representing amorphous or low crystallinity materials, decreases in the order VHSA-G > Fe-K-Q > H-sand, and represents less than 1% of the total DCB-extractable iron in H-sand and Fe-K-Q.

Powder XRD diffractograms for VHSA-G, H-sand, and Fe-K-Q are presented in Figure 1. XRD data for VHSA-G is indicative of small particulate goethite, and the broad peaks may obscure the presence of minor amounts of ferrihydrite that is typically produced by the VHSA-G synthesis. Fe-K-Q consists primarily of quartz and kaolinite, with the potential for some illite, neotocite (Fe, Mn, Mg silicate), and microcline. Notable amounts of an unidentified mineral also exist. DCB extraction data (Table 1) indicate that a significant amount of iron exists in these sediments, and the predominance of kaolinite suggests that this iron does not originate within clay minerals. XRD data for the fine fraction (< 63 μm) of Fe-K-Q (Fig. 1, Fe-K-Q inset) yield peaks at 2Θ = ~33, ~54, and ~64 that are indicative of hematite, and provide evidence that hematite is probably present within the smallest size fraction of Fe-K-Q. XRD data for H-sand indicates that this sediment consists primarily of quartz, with traces of hematite (Fig. 1). Further evidence for the presence of hematite comes from previous studies with this mineral (Zachara et al., 1998), where XRD analysis of the <2 um size fraction yielded clear evidence of for the presence of hematite and small amounts of muscovite.

Further mineralogical analyses of VHSA-G and Fe-K-Q were performed using Mössbauer spectroscopy. The "collapsed" sextet feature in the room temperature (RT) Mössbauer spectrum (Fig. 2a) is indicative of small particulate iron oxide minerals (Mørup, 1990), and is mainly assigned to goethite in this study based on results from XRD analyses. The apparent doublet feature at RT may have contributions from ferrihydrite, since both small particle goethite (< ~15 nm; Murad, 1988) and ferrihydrite can display this doublet feature. At 77 K (Fig. 2c), however, ferrihydrite is still a doublet whereas goethite displays a sextet. Therefore, based on the relative areas of these peaks, the VHSA-G contains ~93% goethite and ~7% ferrihydrite by mass. This value is in good agreement with the wet chemical data (ferrihydrite is soluble in 0.5 N HCl, whereas goethite is only sparingly soluble), but the reader is cautioned that ferrihydrite (SA > ~200 m^2/g) may constitute a much larger proportion of the overall surface area of this goethite-ferrihydrite mixture. The derived Mössbauer parameters for the 77-K spectrum (δ = center shift, Δ/ε = quadrupole shift/quadrupole shift parameter, and B_{hf} = hyperfine magnetic field) for these two iron minerals are (i) δ = 0.48 mm s^{-1} and Δ = 0.61 mm s^{-1} for ferrihydrite, and (ii) δ = 0.49 mm s^{-1} and ε = −0.10 mm s^{-1}, and B_{hf} = 47.3 Tesla for goethite. These parameters are characteristic for these minerals (Murad, 1988).

Comparison of the RT Mössbauer spectrum for the Fe-K-Q uninoculated control (Fig. 2b) with the 77 K Mössbauer for this same sample (Fig. 2d) reveals that the central doublet has contributions from both the phyllosilicate Fe^{III} and iron oxides. The sextet in the 77-K (~72% of area) spectrum is attributable to Fe^{III} oxide minerals (e.g., Kukkadapu et al., 2001). This inference is supported by the large amount of citrate dithionite (DCB) extractable iron found in this sediment (Table 1), and the identification of hematite in this sediment (Fig. 1). The lack of 0.5 N HCl extractable iron in Fe-K-Q (Table 1) indicates that the central doublet in the 77K Mössbauer spectrum of the Fe-K-Q control (Fig. 2d) does not reflect the presence of ferrihydrite. The XRD data indicates the potential presence of various clay minerals that can contain structural iron. Thus, this doublet likely reflects Fe^{III} that is associated with silicates. The extremely small amount of Fe^{II} in the Fe-K-Q uninoculated control (Fig. 2d, offset doublet, ~2% of total Fe) supports this conclusion, as most iron-bearing silicates contain both Fe^{II} and Fe^{III}. XRD data for the fine fraction (< 63 μm) of Fe-K-Q (Fig. 1) display peaks at 2-*theta* = ~9, ~18.5, and ~27.5, which may be indicative of illite.

The exact identity of the iron-bearing minerals in Fe-K-Q cannot be conclusively determined with the current data set. However, the Mössbauer and XRD spectra are consistent with sediment in which 25%–30% (by mass) of the total iron is associated with aluminosilicates and the remaining 70%–75% is associated with small particulate iron oxides that are proba-

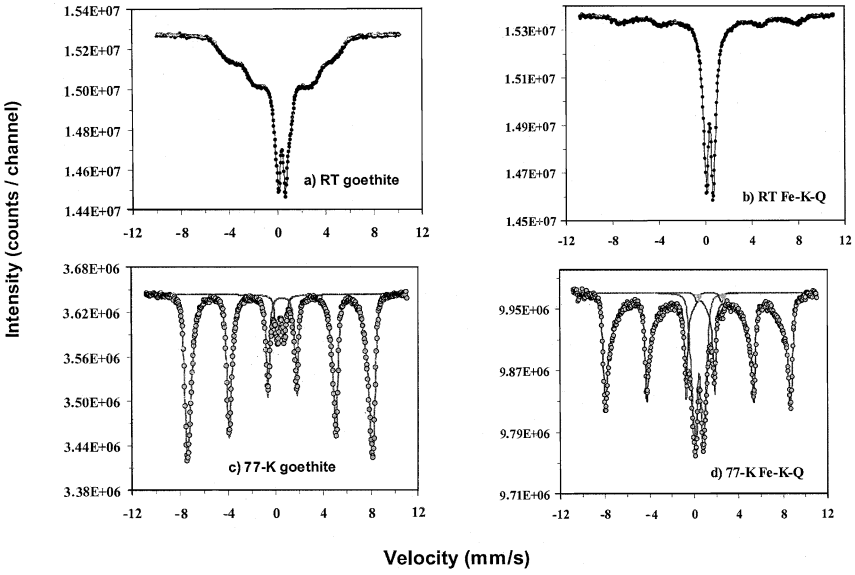

Fig. 2. Room temperature (RT) and 77 K Mössbauer spectra for uninoculated controls of VHSA-G and Fe-K-Q (Fe-K-Q) in the presence of ~225 μM Zn^{II}. (a) VHSA-G at RT, (b) Fe-K-Q at RT, (c) VHSA-G at 77 K, (d) Fe-K-Q at 77 K. (c, d) Gray peaks indicate regions of the 77 K spectrum that are attributed to Fe^{II}; points represent data collected and lines equal model fits. (a, b) Points and line represent the same data set.

bly hematite. Thus, it is likely that the Fe^{III} in this sediment is primarily associated with hematite, kaolinite, and illite. Other iron oxide minerals (e.g., goethite, ferrihydrite) may be also be present, but cannot be conclusively identified. The iron in the H-sand also is predominantly associated with hematite (Zachara et al., 1998), and both Fe-K-Q and H-sand contain low amounts of 0.5 M HCl extractable iron (less than ~1% of total DCB-Fe). Thus, the main difference between these two natural sediments is in the grain size distribution and proportion of clay minerals. The main difference between the two natural sediments and the VHSA-G is in the identity of the primary iron oxide mineral (goethite vs. hematite) and the proportion of ferrihydrite (~7% vs. <1%).

3.2. Effect of Sediment Mineral Composition on Microbial Iron Reduction

Fe^{II} production data for VHSA-G, H-sand, and Fe-K-Q incubated with pure cultures of *S. putrefaciens* 200 are presented in Figure 3, and display trends that are commonly observed in similarly designed batch experiments (e.g., Urrutia et al., 1998; Liu et al., 2001; Roden and Urrutia, 2002). Fe^{II}-sum represents the sum of aqueous and 0.5 M HCl extractable Fe^{II} (Fe^{II}-bound). Most Fe^{II} was produced during the first 200 h, and then continued at a slower rate for several hundred h, effectively stopping by 600 to 700 h. H-sand was reduced to a lesser and more variable extent, and Fe^{II} in these cultures increased more slowly. No increase over time in Fe^{II} was observed in the uninoculated sediments (data not shown). In all sediment slurries, the proportion of bound Fe^{II} was much greater than aqueous Fe^{II}, and solution pH decreased from ~7.2 to ~6.8 over the course of the experiments. Mass and surface area normalized Fe^{II} production rate data are given in Table 2. These data indicate that the surface area normalized Fe^{II} production rates for VHSA-G, Fe-K-Q and H-sand are similar, while the sediment mass normalized rates are not. This discrepancy arises from the different masses of sediment needed to achieve 50 mM DCB-iron in all experiments (see Methods). The similarity in the surface-area normalized Fe^{II} production rates for these different sediments is consistent with

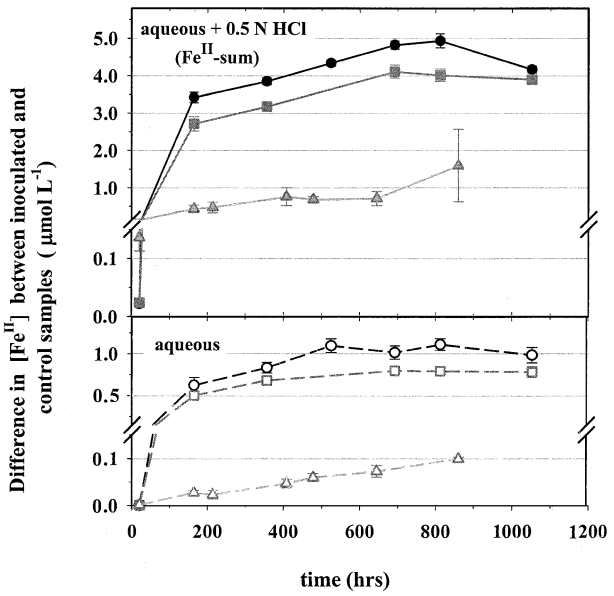

Fig. 3. Fe^{II} generation as a function of time during sediment reduction by *S. putrefaciens*. Note the split axes. Open symbols represent Fe^{II}-aq (bottom), solid symbols represent sum of aqueous and 0.5 N HCl-soluble, surface-bound Fe^{II} (top). Circles = VHSA-G. squares = Fe-K-Q. triangles = H-sand. Data are normalized by subtracting values from uninoculated controls, and error bars represent the standard deviation of three replicate samples.

Table 2. Initial Fe^{II} production rates for VHSA-G, Fe-K-Q and H-sand following reduction by *S. putrefaciens*. Initial rate data are provided for aqueous and Σ aqueous + 0.5 M HCl-soluble Fe^{II} (Fe^{II}-sum).

	VHSA goethite	Fe-kaolinite-quartz	Hematite sand
Fe^{II}-aq production (μmol g-sediment^{-1} h^{-1})	0.7 ± 0.2	0.04 ± 0.01	1.5 ± 0.24 × 10^{-3}
Fe^{II}-sum production (μmol g-sediment^{-1} h^{-1})	3.4 ± 1.3	0.2 ± 0.08	0.02 ± 0.006
Fe^{II}-aq production (μmol m^2-sediment^{-1} h^{-1})	5.6 ± 1.2 × 10^{-3}	1.0 ± 0.3 × 10^{-3}	0.7 ± 0.11 × 10^{-3}
Fe^{II}-sum production (μmol m^2-sediment^{-1} h^{-1})	0.03 ± 0.01	0.005 ± 0.002	0.01 ± 0.003

the general consensus that the degree of "microbial reducibility" of a sediment is primarily a function of its reactive surface area (Roden and Zachara, 1996; Zachara et al., 1998).

3.3. Effect of Sediment Mineral Composition on DMRB-Induced Changes in Iron and Zn^{II} Geochemistry

Analysis of XRD data from 24 "filter cake" samples of microbially reduced sediments (four inoculated, four uninoculated per sediment) revealed no measurable change in mineral composition as a result of microbial Fe^{III} reduction for H-sand and Fe-K-Q (data not shown). However, the color of the Fe-K-Q was observed to darken towards a greenish-brown hue upon microbial reduction. Microbial reduction of VHSA-G did not produce siderite or green rust (XRD data not shown), but did result in some changes in XRD peak shape that are generally similar to, though lesser in magnitude than, those obtained in previous experiments involving goethite reduction by *S. putrefaciens* 200 in this AGW medium (Cooper et al., 2000). Comparison of the RT Mössbauer data for sterile VHSA-G (Fig. 2a) and microbially reduced VHSA-G (Fig. 4a) shows presence of biogenic Fe(II) in the reduced sample (<5% area, Fig. 4a; peaks are indicated by arrows). Its apparent Mössbauer parameters do not reflect the presence of siderite or crystalline green rust, confirming the observations from XRD. RT and 77-K Mössbauer data from VHSA-G that has been reduced and reoxidized via exposure to the atmosphere (Fig. 4b, 4c) shows loss of the Fe^{II}, indicating that the Fe^{II} produced in these experiments is readily oxidized and likely present as adsorbed Fe(II) or a highly reactive mineral phase. Comparison of the 77-K Mössbauer data for sterile VHSA-G (Fig. 2c) with the VHSA-G that has been reduced and reoxidized (Fig. 4c) indicates loss of ferrihydrite during the reduction and reoxidation process. The 77 K Mössbauer spectrum for the microbially reduced Fe-K-Q (Fig. 5a) is similar to the spectrum for the uninoculated controls, the main difference being an increase in the relative proportion of Fe^{II} (to ~5% of total Fe). This magnitude of increase agrees reasonably well with the measurements of Fe^{II} production from wet chemical techniques (Fig. 3). When reduced Fe-K-Q is allowed to reoxidize at ambient atmosphere, the 77 K Mössbauer spectrum (Fig. 5b) is indistinguishable from that of the unreduced controls (Fig. 2d). This again suggests that stable Fe^{II} minerals are not formed, and that Fe^{II} is present as an adsorbed phase. Furthermore, since previous research has indicated that structural Fe^{II} in bio-reduced illite clay is resistant to oxidation in dry air (Dong et al., 2003), the ephemeral nature of Fe^{II} in these experiments indicates that structural Fe^{III} within these illite and kaolinite clays was probably not reduced to a significant extent. The similarity in the 77-K Mössbauer spectra for sterile Fe-K-Q (Fig. 2d) and reduced/reoxidized Fe-K-Q (Fig. 5b) stands in contrast to the VHSA-G, and indicates that microbial Fe^{III} reduction did not irreversibly alter Fe^{III} speciation within Fe-K-Q.

Data presented in Figure 6 demonstrate the effect of microbial iron reduction on the distribution of Zn^{II} in sediment slurries of VHSA-G, Fe-K-Q, and H-sand. DMRB activity increased the concentration of aqueous Zn^{II} in the VHSA-G by 2.0 μM, but did not significantly alter the [Zn^{II}-aq] in the H-sand and Fe-K-Q. Microbial reduction of Fe^{III} bound within Fe-K-Q and H-sand had no consistent effect on the dilute acid (0.5 M HCl) solubility of previously adsorbed Zn^{II} (Fig. 6, middle panel). In contrast, microbial reduction of VHSA-G resulted in the incorporation of Zn^{II} into a 0.5 M HCl insoluble authigenic phase (Zn^{II} strongly bound) (Fig. 6, top and middle panels). This phenomenon has been previously reported for microbial goethite and lepidocrocite reduction in the presence of previously adsorbed Zn^{II} (Cooper et al., 2000). Because the observed Zn^{II} immobilization in VHSA-G resulted from microbial iron reduction, and previous research has indicated that surface area exerts a strong influence on the rate and extent of microbial reduction of synthetic oxide minerals, we repeated the Zn^{II} experiments on synthetic oxides of varying surface area. These synthetic oxides also contained varying amounts of 0.5 M HCl soluble Fe^{III} (~ferrihydrite analog), and the amount of acid soluble Fe^{III} generally increased with increasing surface area (data not shown). Data from surface area experiments presented in Figure 7, indicate that the degree of DMRB-induced Zn^{II} immobilization increases with both surface area and extent of iron reduction. The surface area plot shows a decrease in the degree of Zn^{II} immobilization at the highest surface area, a feature that is not seen when this data are expressed in terms of extent of iron reduction. This accounting of interexperimental differences in DMRB activity reveals that the degree of Zn^{II} immobilization in synthetic oxides is more closely linked to the extent of iron reduction than to mineral surface area. Microbial hematite reduction did not result in Zn^{II} immobilization, mirroring the results from experiments with Fe-K-Q and H-sand. Thus, the Zn^{II} immobilization effect must arise from a variable constituent found within the synthetic VHSA-G and not within synthetic hematite, Fe-K-Q, or H-sand.

Ferrihydrite is present within VHSA-G, but is not present at significant levels within synthetic hematite, H-sand, or Fe-K-Q. Acid extractions of the various synthetic goethite samples revealed that the proportion of 0.5 M HCl soluble Fe^{III} increased with increasing surface area, suggesting that ferrihydrite content also increased with increasing surface area. Thus, we hypothesized that ferrihydrite content might affect the de-

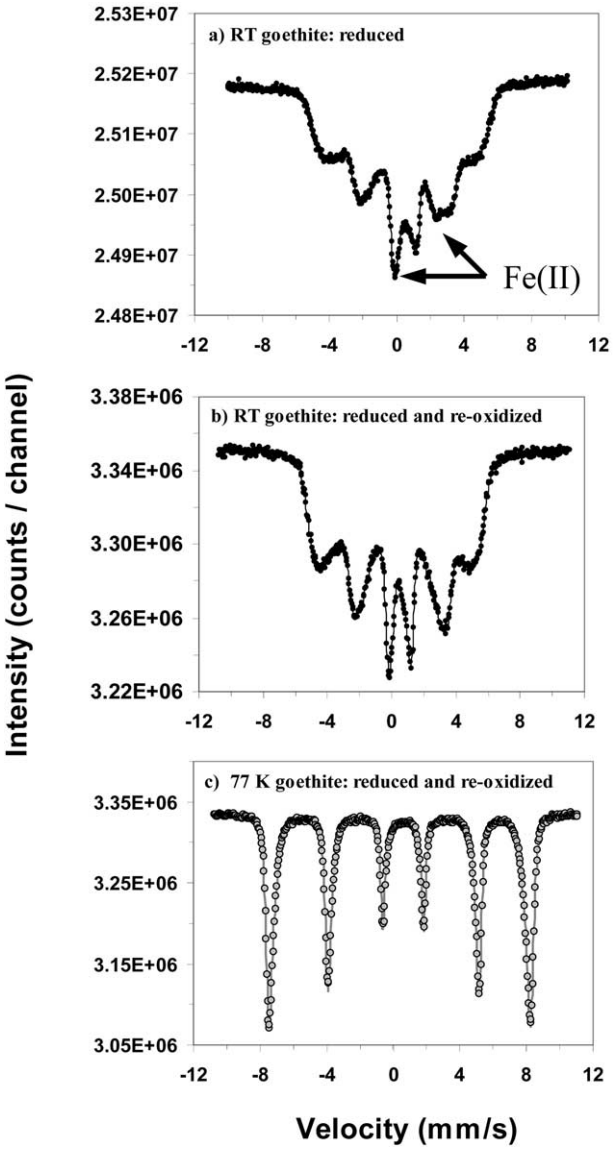

Fig. 4. Room temperature (RT) and 77 K Mössbauer spectra of microbially reduced VHSA-G and microbially reduced VHSA-G that has been reoxidized. All samples are in the presence of 225 μM Zn^{II}. (a) RT reduced, (b) RT reduced and reoxidized, (c) 77 K reduced and reoxidized. Marked peaks indicate regions of the RT spectra that are enhanced by Fe^{II} generation. (a, b) Points and line represent the same data set. (c) Points represent data and line equals model fit for goethite.

gree of Zn^{II} immobilization that was observed to occur during microbial reduction of synthetic goethite. Data from an experiment to test this hypothesis are presented in Figure 8. In this experiment, varying amounts of ferrihydrite were added to LSA goethite, hematite, or Fe-K-Q as described in the Methods. Ferrihydrite addition greatly increased the degree of Zn^{II} immobilization for synthetic hematite and low surface area (LSA) goethite, but the effect of ferrihydrite addition was so small as to be inconsequential in the Fe-K-Q. Thus, while these data indicate that the degree of Zn^{II} immobilization into a strongly bound phase (0.5 M HCl insoluble) can be enhanced via addition of ferrihydrite to all sediment systems tested, they also indicate that other aspects of sediment mineral composition can greatly mitigate this effect.

3.4. Effect of Sediment Mineral Composition on DMRB-Induced Changes in Zn^{II} Speciation: X-ray Absorption Spectroscopy

The chemical extraction data presented previously provide strong evidence that microbial Fe^{III} reduction can induce dramatic changes in Zn^{II} speciation within an iron-bearing sediment, and that the magnitude of this change increases with the ferrihydrite content. Thus, microbial reduction of ferrihydrite in the VHSA-G and ferrihydrite-amended sediment systems may result in formation of 0.5 M HCl insoluble iron oxide minerals, and incorporation of previously adsorbed Zn^{II} into their crystal structure. This hypothesis is consistent with previous reports (see "Discussion"), and was tested by collecting Zn^{II} *k*-edge XANES and EXAFS spectra for the VHSA-G and Fe-kaolinite quartz systems. These sediments were chosen for further analysis because (1) they provided contrasting behavior in Zn^{II} speciation, (2) they were the most comparable in terms of iron

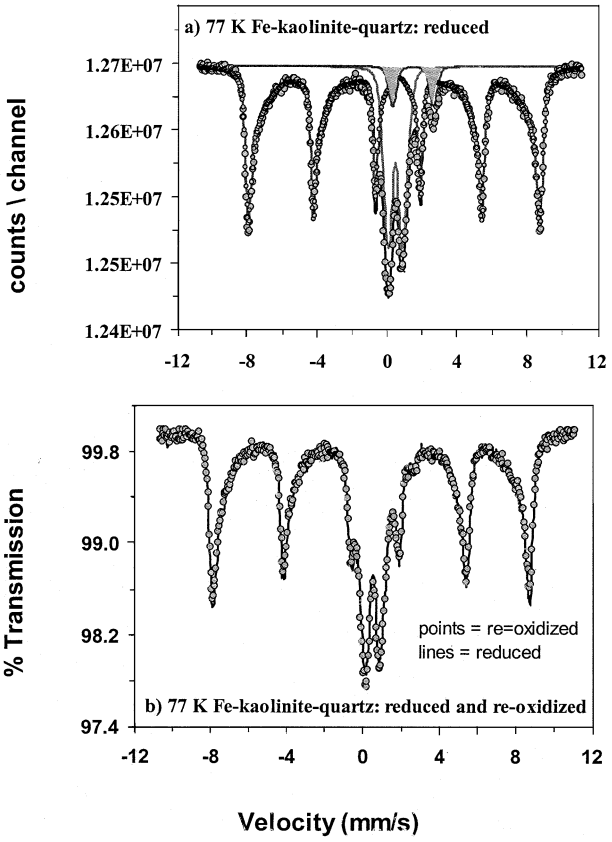

Fig. 5. 77 K Mössbauer spectra of microbially reduced Fe-K-Q and microbially reduced Fe-K-Q that has been reoxidized. All samples are in the presence of 225 μM Zn^{II}. (a) 77 K reduced; (b) comparison between uninoculated Fe-K-Q and Fe-K-Q that has been reduced and reoxidized (77 K). (a) Gray peaks indicate regions of the 77 K spectrum that are attributed to Fe^{II}, points represent data collected, and lines equal model fits. (b) Line represents data for sterile, unreduced Fe-K-Q and points represent reduced and reoxidized Fe-K-Q.

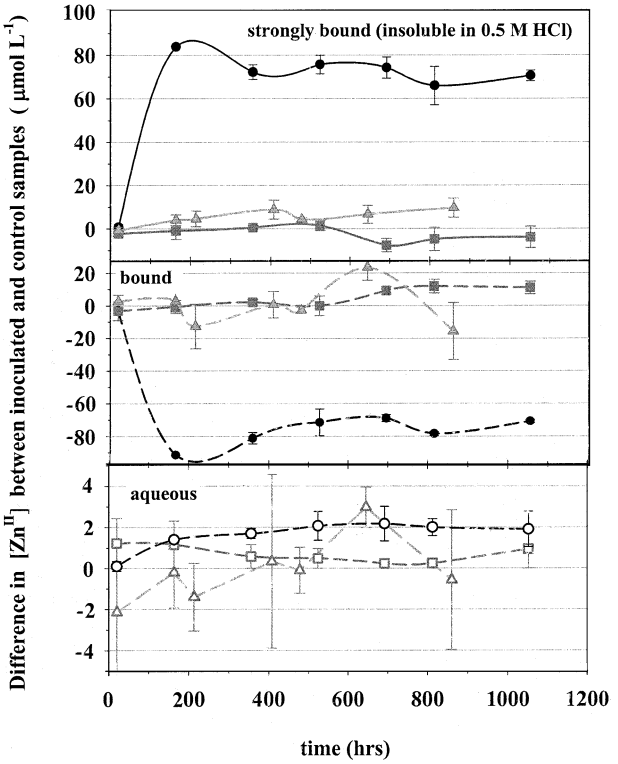

Fig. 6. Plot of Zn^{II} speciation as a function of time. Open symbols represent aqueous Zn^{II} (bottom), solid symbols with dotted lines represent weakly bound Zn^{II} (soluble in 0.5 M HCl, middle), and solid symbols with solid lines represent strongly bound Zn^{II} (insoluble in 0.5 M HCl but soluble in 6 M HCl), top). Circles = VHSA-G, squares = Fe-K-Q, triangles = H-sand. Data are normalized by subtracting values from uninoculated controls, and error bars represent the standard deviation of three replicate samples.

content and overall extent of Fe^{III} reduction, and (3) beam-time considerations limited us to two sediments.

Zn^{II} *K*-edge XANES collected from sterile and inoculated goethite surfaces (Fig. 9) are similar, with a strong white line at ~9670 eV and a secondary feature ~19 eV above the edge. A similar near-edge structure is, as Waychunas et al. (2002, 2003) observed, common to many complexes and structures containing octahedrally coordinated transition metals, including zinc. The position of the secondary feature is consistent between the sterile controls and inoculated goethite samples, but is more pronounced in spectra collected from VHSA-G inoculated with *S. putrefaciens.* In a calculation of the XANES from a cluster of edge-sharing ZnO_6 octahedra, Waychunas et al. showed that this feature became more defined as the available multiple scattering paths increased upon addition of octahedra to the cluster. Thus, the XANES of the inoculated sample is consistent with enhanced multiple scattering compared to the sterile sample, possibly resulting from larger clusters or increased order in the structure. This feature can arise from a number of different structures, and will be discussed further in subsequent sections.

The k^3-weighted EXAFS spectrum for the sterile goethite (Fig. 10) is dominated by a single wave frequency, suggesting a single ordered coordination sphere around the central Zn^{II}. The k^3-weighted EXAFS spectrum for the inoculated goethite is similar, though there are some small but significant differences at higher frequencies. Fourier transforms (k^3-weighted, not corrected for phase shift) obtained over a *k*-range of 0.5–10 $Å^{-1}$, with a Kaiser-Bessel window (de-emphasizing the ends of the data) are shown in Figure 11, exhibiting dominant near-neighbor peaks for both samples. Small secondary peaks are visible in both sterile and inoculated samples. These peaks are above the noise level, and are more pronounced in the inoculated sample. This difference may arise from increased multiple scattering (as in the XANES data), or could possibly reflect a slightly increased degree of single scattering from Zn^{II}-metal second shell interactions. The data are not conclusive in this regard, and alternative interpretations will be examined in subsequent sections.

EXAFS modeling parameters are provided in Table 3. Fourier-transform fitting procedures were the same as in the previous figures, and fitting was performed over the range 0.5–2.0 Å. The limited data available required constraints on the number of floating variables to remain within the limits dictated by the number of independent data points. Reasonable results for both goethite surfaces (shown in Table 3A) were obtained with a model consisting of subshells of oxygen atoms whose coordination numbers were fixed at a ratio of 2:1, while varying total coordination ($N = N_a + N_b$). R of each subshell was allowed to vary, as were a common E_0 and a common σ^2. Fits with individually varying σ^2 were also attempted, as were fits with other ratios of N_a and N_b, but the calculated uncertainties and the goodness-of-fit parameter, χ^2_ν were degraded (results not shown). The results of modeling suggested that in both cases the Zn^{II} nearest-neighbors were oxygen. There is an indication that coordination number (CN) increased from 5 for

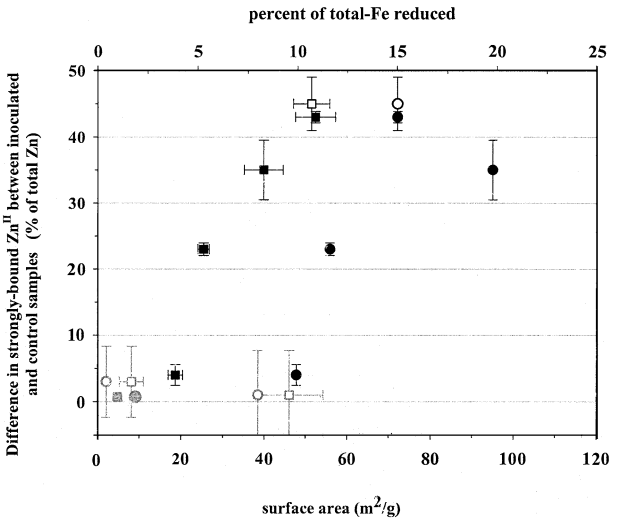

Fig. 7. Plot of Zn^{II}-strongly bound (0.5 M HCl insoluble, but soluble in 6 M HCl) as a function of mineral surface area (circles, bottom axis) and percentage of total-Fe reduced (squares, top axis) for synthetic goethite reduced by *S. putrefaciens* (solid circles, squares), synthetic goethite reduced by *G. metallireducens* (open circles, squares), synthetic hematite reduced by *S. putrefaciens* (solid gray circles, squares), and natural sediments reduced by *S. putrefaciens* (open gray circles, squares). Data are normalized by subtracting values from uninoculated controls, and error bars represent the standard deviation of three replicate samples.

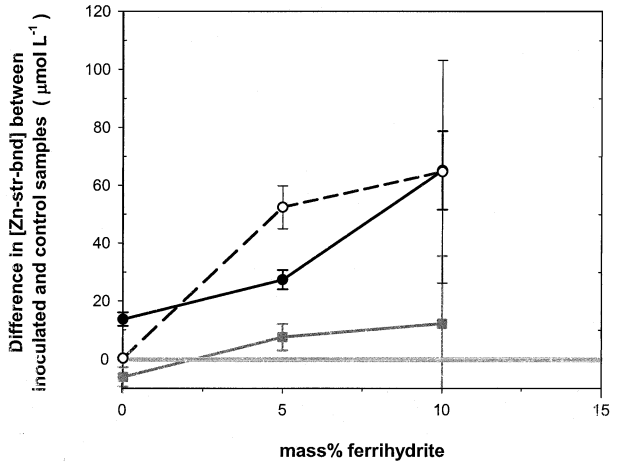

Fig. 8. Plot of Zn^{II}-strongly bound (0.5 M HCl insoluble, but soluble in 6 M HCl) vs. mole percent ferrihydrite for synthetic LSA goethite (solid circles), synthetic hematite (open circles), and sediment Fe-K-Q (solid squares). Data are normalized by subtracting values from uninoculated controls.

Zn^{II} associated with sterile goethite samples to 6 for Zn^{II} associated with inoculated goethite samples, but the difference in the model fit may not be significant, given the uncertainties in the results. It is important to note that, even given these uncertainties in model fitting parameters, there are real differences in the spectra of the inoculated and sterile samples in the XANES and EXAFS spectra. These differences coincide with large changes in the acid solubility of Zn^{II}. Thus, while the data are too sparse to fully describe the changes in Zn^{II} bonding structure, differences are evident.

In contrast to the subtle differences observed in the XANES spectra of the VHSA-G samples, striking differences were observed in the XANES spectra collected from the sterile and inoculated Fe-K-Q samples (Fig. 9). The near-edge spectrum of the sterile sample is similar to those observed for goethite samples, exhibiting characteristic octahedral XANES edge-structure. The sterile sample also contains a secondary peak at approximately equivalent energy, relative to the edge, as is found with goethite. This secondary peak is more pronounced than in goethite, indicative of higher orders of multiple scattering. The near-edge region of the spectrum collected from inoculated Fe-K-Q displays three well-defined edge features, and is quite distinct from the structure collected from uninoculated Fe-K-Q. This feature is characteristic of transition metals in tetrahedral coordination (Waychunas et al., 2002, 2003). The k^3-weighted EXAFS spectra (Fig. 10) for both sterile and inoculated Fe-K-Q again suggests differences exist between the two treatments, with a distinctly different dominant frequency, and larger amplitude at higher k for inoculated samples. The k^3 Fourier Transforms (Fig. 11) bear these observations out, as the near-neighbor peak in the inoculated sample is larger and shifted to larger R.

Modeling the Zn^{II} local structure in the sterile Fe-K-Q samples again suggested there were similarities between it and the two goethite samples with best fit being derived from oxygen as the nearest neighbor and a CN of 5 (Table 3A). Attempts to model the Zn^{II} local structure in the Fe-K-Q sample in the presence of *S. putrefaciens* indicates that Zn^{II} coordination is significantly different from the other spectra, supporting the conclusion reached from examining the XANES and Fourier transforms. In this case, a reasonable model incorporating oxygen neighbors could not be found. One conceivable possibility is a highly unconstrained, mixed oxygen environment composed of multiple Zn-O bond geometries. However, this is difficult to reconcile with the observation that the FT peak in this system is significantly shifted to larger R, given that Zn-O bond lengths are typically similar. The increased strength of the FT peak and shift to larger R suggests the possibility of a larger, heavier neighbor, but a likely candidate is not entirely clear. For instance, the FT peak from a Zn-Zn bond would be apparent at $R \sim 2.3$ Å and a Zn-Fe bond would likely behave similarly. A best fit to the Fe-K-Q data in the presence of *S. putrefaciens* was achieved by using a $ZnCl_2$ structure (CN = 5, see Table 3B). Various Zn-S structures (e.g., $ZnSO_4$, ZnS) were also examined, but EXAFS modeling did not yield a good fit for models based on Zn-S associations (data not shown). The Zn-O models each produced results that were physically unrealistic, for example, extremely large E_0 shifts, negative σ^2, etc. As the results of fitting the various models suggest, varying the window over which the Fourier transform was performed did not result in improvements to the Zn-O (or Zn-S) models such that they represented a better fit to the data or produced physically realistic parameter values, and Zn-Cl first shell neighbors remain the best description of the data. However, a small Zn-O (or Zn-S) contribution cannot be discounted since the fit improved quite substantially when the lowest k-range was excluded. This would indicate a lower-Z neighbor (e.g., oxygen, sulfur) may be contributing to the EXAFS besides chlorine.

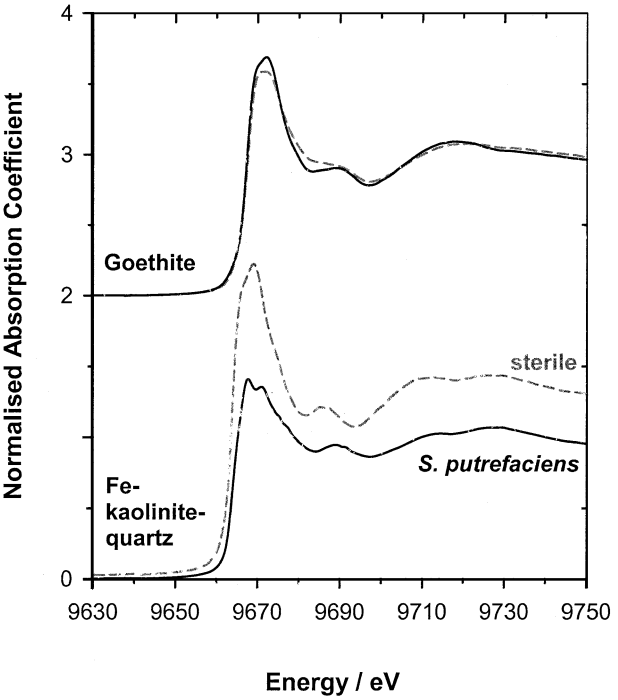

Fig. 9. XANES for sterile VHSA-G (upper half, dashed line), inoculated VHSA-G (upper half, solid line), sterile Fe-K-Q (lower half, dashed line), and inoculated Fe-K-Q (lower half, solid line).

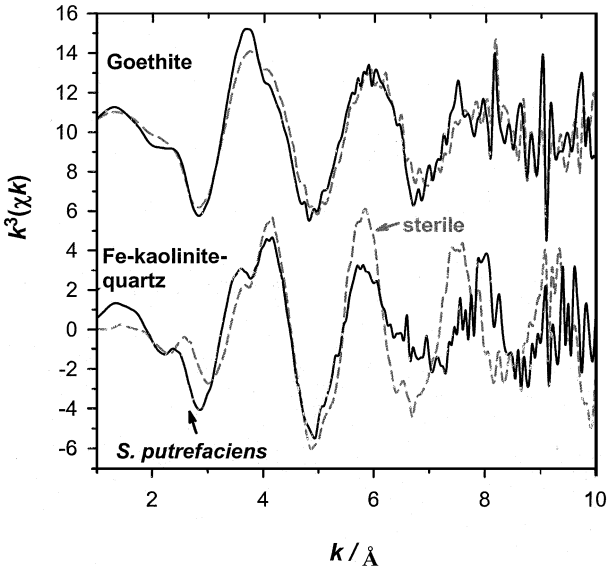

Fig. 10. k^3-weighted EXAFS for sterile VHSA-G (upper half, dashed line), inoculated VHSA-G (upper half, solid line), sterile Fe-K-Q (lower half, dashed line), and inoculated Fe-K-Q (lower half, solid line).

Determining the details of this structure will likely depend on the acquisition of additional data with improved S/N ratio.

The fitting results summarized in Table 3 broadly support the conclusions reached by examining the XANES and Fourier Transforms; the Zn^{II} environment is similar in the goethite systems and the sterile Fe-K-Q system. There is a slight difference between the goethite samples in the results for *N*, but the magnitude of this change is similar in magnitude to the uncertainties associated with the fitting procedure. It should be noted that the fitting results reflect the difficulty in modeling a fairly complicated structure with a limited data set. In particular, note the large uncertainties in σ^2 and *R*, which are produced by the large correlation between these variables in a two-shell fit (the *k*-dependent beating produced by two closely spaced shells mimics the behavior of the gaussian factor in which σ^2 appears). However, *N* was obtained with reasonable certainty because the fit included small *k* values, where the effect of σ^2 is small and the two shells are nearly in phase. The results for *N* were also relatively insensitive to the details of the model (changing by less than 10% in each case when independent σ^2 for the two subshells). Overall, the fitting results in combination with the qualitative comparison of the XANES and Fourier transforms produce confidence in the conclusions that:

1. There are real differences in the XAS spectra of the sterile and inoculated VHSA-G samples. However, the changes are too small to allow a full quantitative description of the two different structures with current data.
2. The Zn^{II} environment in the goethite and sterile Fe-K-Q samples is similar.
3. The Zn^{II} environment in the inoculated Fe-K-Q sample is distinct from the sterile sample, and current data suggest a shift from octahedral Zn-O to tetrahedral $ZnCl_2$.

4. DISCUSSION

Surface area normalized rates of Fe^{II} production are similar for all sediments tested, and thus these data agree with previous investigations into the effect of surface area on the degree of "microbial reducibility" (e.g., Roden and Zachara, 1996; Zachara et al., 1998). Our data are also consistent with previous studies indicating that the presence of nonreducible minerals does not notably affect the "microbial reducibility" of sedimentary iron oxides (Zachara et al., 1998). However, while our data support previous conclusions, they also demonstrate that the geochemical properties of sedimentary minerals (e.g., crystal structure, surface chemistry) place a primary control on the effect of microbial iron reduction on iron and Zn^{II} speciation. More specifically, our data indicate that (1) the presence of nonreducible sedimentary minerals can mitigate the effect of microbial Fe^{III} oxide reduction on Zn^{II} speciation, and (2) ferrihydrite plays a central role in mediating the geochemical effect(s) of microbial iron reduction.

4.1. Importance of Nonreducible Minerals

These data indicate that the presence of nonreducible sedimentary minerals can mitigate the effect of microbial Fe^{III} oxide reduction on Zn^{II} speciation. Microbial Fe^{III} reduction in VHSA-G increased the [Zn^{II}-aq] and engendered large changes in the proportion of 0.5 M HCl soluble Zn^{II}. Similar changes were not observed in Fe-K-Q and H-sand. In the ferrihydrite addition experiments, ferrihydrite addition notably increased the proportion of 0.5 M HCl insoluble Zn^{II} in systems where VHSA-G and synthetic hematite were microbially reduced. In Fe-K-Q, where nonreducible iron-bearing minerals are present, ferrihydrite addition had a much smaller effect on Zn^{II} speciation. Thus, while the presence of nonreducible minerals minimally affects the ability for a DMRB to utilize Fe^{III} oxides in nutrient rich conditions, these minerals can significantly alter

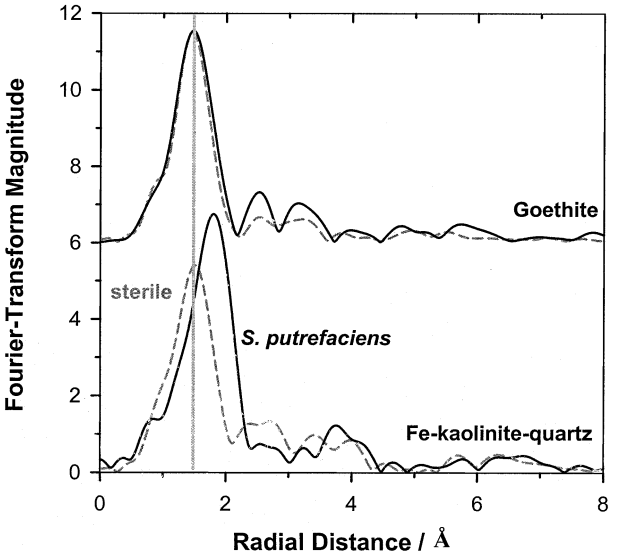

Fig. 11. Fourier Transforms of k^3-weighted EXAFS of sterile VHSA-G (upper half, dashed line), inoculated VHSA-G (upper half, solid line), sterile Fe-K-Q (lower half, dashed line), inoculated Fe-K-Q (lower half, solid line).

Table 3. Results of fitting in *R*-space of the first neighbor shell. Uncertainties in the fitted parameters are shown in parentheses.[a]

(A)

Sample	$N = N_a + N_b$	ΔE_0 (eV)	R_a (Å)	R_b (Å)	σ^2 ($\times 10^{-3}$ Å^2)	χ^2_ν
Goethite	4.9 (0.6)	−5.2 (1.5)	2.03 (0.01)	1.89 (0.04)	4.2 (4.0)	5.9
Goethite + *S. putrefaciens*	6.2 (0.7)	−3.9 (1.3)	2.07 (0.02)	1.94 (0.08)	9.1 (7.0)	2.9
Fe-kaolinite-quartz	5.3 (0.6)	−4.5 (1.9)	2.05 (0.01)	1.89 (0.03)	3.1 (2.9)	7.1

(B)

Model/fitting range	$N = N_a + N_b$	ΔE_0 (eV)	ΔR_a	ΔR_b	σ^2 ($\times 10^{-3}$ A^2)	χ^2_ν
Zn-Cl/3-11	5.0 (1)	2.1 (2.3)	0.01 (0.02)	—	10.2 (2.2)	16
Zn-O/3-11	5.0 (1.7)	21.1 (3.1)	0.06 (0.02)	—	5.0 (3.5)	54
Zn-O/0.5-9	4.3 (1.8)	17.4 (3.7)	0.03 (0.03)	—	3.1 (5.5)	362
Zn-O 2:1 split/3-11	4.0 (1.3)	11.1 (3.9)	0.07 (0.03)	−0.08 (0.04)	−3.1 (3.2)	59
Zn-O 2:1 split/0.5-9	3.3 (1.2)	9.2 (4.0)	0.05 (0.04)	−0.12 (0.06)	−7.4 (.005)	333

(A) Results of fitting O first neighbors to the sterile and inoculated goethite samples and sterile Fe-K-Q.

(B) Results of fitting Cl or O first neighbors for inoculated Fe-K-Q. ΔR is the difference in the fitted distance compared to the standard. Standard for the Zn-Cl model was a fourfold Zn-Cl shell with bond length of 2.28 Å, based on $ZnCl_2$. The Zn-O standards were two shells with fourfold and twofold coordination and bond length 2.11 Å (total $N = 6$), based on $ZnCO_3$. The 0.5–9 fitting condition is the same as that which produced the results for the other samples.

[a] Fitting was performed with N_a constrained to be $N_b \times 2$. E_0 and σ^2 were constrained to be equal for each subshell. χ^2_ν is defined as χ^2 divided by the difference between the number of independent points in the data and the number of quantities varied in the fit: $\chi^2/(N_{ind} - N_{var})$.

the effect(s) of microbial Fe^{III} reduction on metal geochemistry.

Mössbauer spectroscopy and Zn k-edge XAS data collected from VHSA-G and Fe-K-Q samples aged under sterile and inoculated conditions also support this conclusion. In VHSA-G, DMRB activity preferentially removed ferrihydrite and induced subtle shifts in Zn^{II} bonding structure that dramatically altered Zn^{II} 0.5 M HCl solubility. In Fe-K-Q, DMRB activity did not permanently alter iron speciation and induced dramatic shifts in Zn^{II} bonding structure that had minimal effect on Zn^{II} 0.5 M HCl solubility. This difference is unlikely to result from solution components, as both VHSA-G and Fe-K-Q experienced similar degrees of Fe^{III} reduction. Mössbauer data indicate that DMRB activity did not dissolve clay minerals in Fe-K-Q, enabling these surfaces to potentially mitigate the geochemical effects of microbial iron oxide reduction. If this process were operative in Fe-K-Q, then we would expect microbial Fe^{III} reduction to induce a shift from a Zn-O octahedral coordination reflective of inner-sphere surface complexation with iron oxide minerals (uninoculated Fe-K-Q) to a different coordination more reflective of outer-sphere surface complexes with clay minerals (inoculated Fe-K-Q).

The Zn *k*-edge XANES data for sterile Fe-K-Q suggest that adsorbed Zn^{II} exists in an octahedral structure similar to that observed on the two goethite samples and that some degree of multiedge polyhedra exist (e.g., Waychunas et al., 2003). Upon reduction by *S. putrefaciens*, the near-edge spectra for Fe-K-Q have the appearance of a tetrahedrally coordinated Zn environment as evidenced by the presence of three near-edge features characteristic of such coordination. The near-edge spectra for VHSA-G do not display a similar change. While there can be no question that Zn^{II} adsorbed to Fe-K-Q shifted from an octahedral structure to a tetrahedral structure upon reduction, elucidating the *chemistry* responsible for this transformation is somewhat problematic. Waychunas et al. (2002, 2003) report that a variety of *chemical structures* can produce similar multiple scattering phenomena identifiable by XANES spectroscopy. Qualitative comparison of XANES data for microbially reduced Fe-K-Q with near-edge spectra of hydrozincite ($Zn_5[CO_3]_2[OH]_6$), smithsonite ($ZnCO_3$), ZnS, and $ZnCl_2$ standards (Fig. 12) suggest that the primary near-edge feature at ~9670 eV (inoculated spectrum) is most similar to $ZnCl_2$. The secondary feature observed at ~9690 eV is not easily attributable to $ZnCl_2$, and qualitative comparison suggest that ZnS may be present. However, while this qualitative XANES compari-

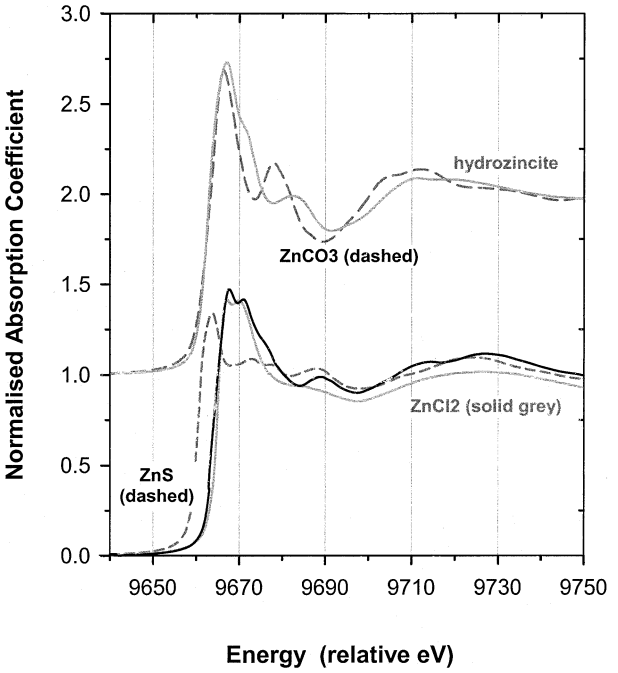

Fig. 12. XANES for inoculated Fe-K-Q (lower, black), $ZnCl_2$ (lower, solid gray), ZnS (lower, dashed), hydrozincite (upper, solid), and $ZnCO_3$ (upper, dashed). Normalized coefficients for $ZnCO_3$ and hydrozincite offset by $y + 1$ for clarity.

son allows for ZnS, the work of Waychunas et al. (2002, 2003) indicates that this secondary structure at ~9690 eV can also arise from an alternative chemistry. This feature may indicate the existence of ZnS or another structure with a similar degree of multiple scattering. XANES cannot provide conclusive characterization of this structure.

Zn EXAFS results for sterile Fe-K-Q are similar to those for VHSA-G, and agree with the XANES data set in this regard. The sterile data set is best modeled by a split first shell of oxygen with a CN of 5 (Table 3A). Little evidence exists for higher shells, suggesting an absence of inner-sphere (IS) surface complex formation or incorporation of Zn^{II} into phyllosilicates in Fe-K-Q (*sensu* Schlegel et al., 2001; Manceau et al., 2002). EXAFS modeling of the inoculated system indicates that microbial iron reduction engenders a transformation from octahedral Zn^{II} to tetrahedral Zn^{II} in Fe-K-Q, while no such change is observed in VHSA-G. These data also provide support for the formation of $ZnCl_2$ in the reduced Fe-K-Q (Table 3B), and the agreement between XANES and EXAFS analyses indicates that $ZnCl_2$ is the dominant structure in the microbially reduced Fe-K-Q. The chemistry associated with the secondary features is still unresolved. The secondary feature at ~9690 eV (Fig. 12) may arise from ZnS, or it may arise from multiple scattering associated with a limited secondary contribution from Zn-O moieties. The AGW medium did not contain any reduced sulfur, *S. putrefaciens* 200 is not capable of SO_4^{2-} reduction, and we observed no indication of sulfide formation. Thus, ZnS formation is unlikely and chemical considerations provide more support for a limited Zn-O contribution.

The formation of $ZnCl_2$ is perplexing, since thermodynamic calculations based on bulk chemical composition provide little support for the formation of this phase. Due to a lack of appropriate complexation constants, these calculations ignored the effect of Zn^{II}-organic complexes. Thus, it is possible that Zn-organic moieties could alter Zn^{II} speciation to favor the formation of $ZnCl_2$. Alternatively, mineral surfaces are known to induce formation of complexes and precipitates at much lower aqueous concentrations than predicted by equilibrium models based on bulk solution composition (e.g., Farley et al., 1985; Towle et al., 1997; Waychunas et al., 1999), and it is reasonable to postulate that the diffuse double layer around clay and microbially reduced iron oxide surfaces in the reduced Fe-K-Q is sufficiently different from that of the nonreduced, sterile controls to enable formation of outer-sphere $ZnCl_2$ surface complexes. Some support for this hypothesis can be found in both the secondary peak at ~9690 eV in the XANES spectrum (Fig. 12) and the fact that the EXAFS fit is further improved by allowing Zn^{II} complexation with a small and indeterminate number of atoms lighter than Cl (indicated by removing the lower *k*-space region). This improvement most likely arises from some limited contribution from additional Zn-O moieties that can arise from either a hydrated $ZnCl_2$, or perhaps from some limited site-specific association between Zn^{II} and aluminol/silanol sites on clay mineral edges. Though this hypothesis about the chemical nature of the secondary features in the Zn *k*-edge XAS spectra for microbially reduced Fe-K-Q is somewhat speculative, it is in agreement with all available data—and this chemistry would be expected to occur in a system where Zn adsorption is dominated by the formation of $ZnCl_2$ outer-sphere complexes. The combination of EXAFS modeling and thermodynamic considerations indicates that microbial reduction of Fe^{III} in Fe-K-Q results in the transfer of previously adsorbed Zn^{II} from weak surface complexes with iron oxide minerals to outer-sphere $ZnCl_2$ surface complexes with sedimentary clay minerals. Chemical data indicate that these outer-sphere $ZnCl_2$ surface complexes are not susceptible to acid-based dissolution.

4.2. Importance of Ferrihydrite

These data indicate that the ferrihydrite content of sediment can play a central role in mediating the geochemical effect(s) of microbial iron reduction. VHSA-G reduction did not produce measurable amounts of siderite or other ferrous minerals, when previous investigations of microbial reduction of a different synthetic goethite (SA = 125 $m^2\ g^{-1}$, higher ferrihydrite content) by *S. putrefaciens* 200 in this medium resulted in faster and more complete Fe^{III} reduction and produced siderite and other ferrous minerals (Cooper et al., 2000). This discrepancy may result from differences in ferrihydrite content. In experiments with Al-substituted goethite, Kukkadapu et al. (2001) reported that the rate/extent of Fe^{III} reduction can alter resultant Fe^{II} speciation, and that all Fe^{II} adsorption sites must be exhausted before siderite or green rust precipitation occurs. These authors further assert that increased levels of ferrihydrite can increase Fe^{III} reduction rates and allow formation of siderite and/or green rust. Comparison of the results reported herein with the work of Cooper et al. (2000) indicates that ferrihydrite may alter iron speciation in microbially reduced sediments and lends support to the hypotheses of Kukkadapu et al. (2001).

For all experiments with sediments that contained measurable amounts of ferrihydrite, microbial Fe^{III} reduction increased the proportion of Zn^{II} associated with a 0.5 M HCl insoluble, "strongly bound" phase. This transition was not observed in systems that contained negligible amounts of ferrihydrite. This effect was most pronounced in the VHSA-G experiments, where the only 0.5 M HCl insoluble phase identified was goethite and Mössbauer data indicate that microbial VHSA-G reduction resulted in production of adsorbed Fe^{II} and preferential loss of ferrihydrite. These data suggest that microbial reduction of VHSA-G and other ferrihydrite-bearing systems can result in authigenic goethite formation and precipitation of a Zn-substituted goethite. Previous studies report that presence of Fe^{II} can facilitate the conversion of ferrihydrite to goethite (Andreeva et al., 1995; Hansel et al., 2003; Zachara et al., 2002), and that microbial ferrihydrite reduction can catalyze the transformation of ferrihydrite to goethite in continuous flow systems where the [Fe^{II}-aq] is less than ~0.5 mmol Fe^{II}/g ferrihydrite (Benner et al., 2002; Hansel et al., 2003; Zachara et al., 2002). If this mechanism were operative in our ferrihydrite-bearing systems, we would expect the degree of Zn^{II} incorporation into the 0.5 M HCl insoluble phase to increase with increasing degree of Fe^{II} production and ferrihydrite content. These trends were observed (Figs. 7 and 8). From a mass balance perspective, Cornell and Schwertmann report that Zn^{II} can substitute for Fe^{III} in goethite to a maximum of ~0.07 mol Zn^{II} per mol goethite (Cornell and Schwertmann, 1992). Our microbially reduced VHSA-G contained an average of ~0.004 mol acid-insoluble Zn^{II} per mol DCB-iron, which equates to ~0.06 mol acid-insoluble Zn^{II} per mol ferrihydrite (~7

weight% ferrihydrite in VHSA-G). Thus, at greater than 85% conversion, the VHSA-G contains sufficient ferrihydrite to account for the observed change in Zn^{II} speciation.

Zn k-edge XAS data collected from VHSA-G samples aged under sterile and inoculated conditions provides additional support. If this process were operative, then we would expect microbial Fe^{III} reduction to maintain first order Zn-O octahedral coordination reflective of inner-sphere surface complexation with iron oxide minerals while increasing the degree of second order Zn-O-metal interactions. These changes were observed, but not to the extent expected. Zn *k*-edge XANES data display a change that might result from a shift in the degree of multiple scattering, but of too small a magnitude to be considered conclusive. Modeling of Zn *k*-edge EXAFS data indicates an average Zn-O coordination number of 5, bond length of 2.03 Å, and insignificant second order interactions for sterile VHSA-G (Table 3A, Fig. 11). The Zn-O coordination number and bond length in the sterile system is intermediate between the tetrahedral coordination (CN = 4) and ~1.97 Å bond length reported for Zn^{II} complexation with well crystalline goethite and ferrihydrite (Trivedi et al., 2001; Waychunas et al., 2002) and the octahedral coordination (CN = 6) and ~2.18 Å bond length reported for Zn^{II} complexation with HFO (Trivedi et al., 2001). These Zn *k*-edge XAS data indicate that Zn^{II} in the sterile VHSA-G is either adsorbed to hydrous ferric oxide (HFO) or weakly associated with more crystalline iron oxide minerals. This interpretation is also supported by the absence of second shell interactions in the sterile VHSA-G, commonly interpreted as an indication of outer-sphere (OS) surface complexes (e.g., Strawn and Sparks, 1999; Trivedi et al., 2001; Waychunas et al., 2002). Upon reduction, Zn-O shifts to a predominantly octahedral coordination with slightly longer Zn-O bond lengths (Table 3A). We also observed a slightly increased degree of order, as evidenced by (1) the increased intensity of the near-edge feature at 9685 eV (Fig. 9), (2) subtle differences in the k^3-weighted EXAFS spectrum at higher frequencies (Fig. 10), and (3) a weak increase in second order interactions in the Fourier transformed EXAFS spectra for microbially reduced VHSA-G (Fig. 11). While these changes are small, they are slightly above the level of uncertainty and must be considered significant in light of the concomitant transformations in iron speciation and associated changes in Zn^{II} acid solubility.

Interpreting these changes in light of current knowledge is problematic. Previous reports note significant Zn-Fe second nearest neighbor interactions when Zn^{II} is bound to well crystalline goethite via an inner sphere complex (Trivedi et al., 2001), or when Zn^{II} is coprecipitated with macrocrystalline iron oxide minerals (Waychunas et al., 2002). We did not observe a *strong* increase in the M-M shell (i.e., Zn-Zn and/or Zn-Fe) in the Fourier-transformed EXAFS spectra, and thus there is good reason to doubt that our small changes in second order interactions are reflective of an increase in Zn-O-Fe bonding associated with increased Zn^{II} substitution in goethite. Yet, the combination of (1) the observed changes in Zn^{II} acid solubility, and (2) the preferential loss of ferrihydrite upon reduction argue that these subtle changes in Zn^{II} bonding environment are reflective of such a change. This conflict can only be resolved if either:

1. Zn^{II} is becoming incorporated into an acid-insoluble metal oxide mineral (e.g., goethite), but that the extremely small iron oxide particle size, the presence of crystal defects, and/or the Zn/Fe molar ratio influences the EXAFS contributions by reducing longer range (higher shell) interactions, *or*

2. Differences in microbial response to these two different sediments results in Zn^{II} becoming incorporated into a different acid-insoluble solid phase where a lighter compound, such as phosphorous or sulfur, provides a second nearest neighbor.

Previous investigations of Zn^{II} association with ferrihydrite and goethite (Trivedi et al., 2001; Waychunas et al., 2002) utilized well-ordered crystals. In contrast, the iron oxide minerals in these experiments were poorly ordered microcrystallites, and may display a smaller magnitude of M-M second shell interactions in EXAFS spectra. Menceau et al. (2003) report that zinc oxide nanoparticles embedded within zeolites have a much reduced Zn *k*-edge EXAFS amplitude than bulk zinc oxide, and Greaves et al. (1999) note a similar effect with cadmium oxide nanoparticles. Gerth (1990) suggests that Zn^{II} located within the goethite crystal structure is bound in a highly distorted octahedron where Zn-O bond lengths average ~2.03 Å, which is similar to the average Zn-O bond length value that we report. Waychunas et al. (2002) has suggested that such distortion could create anharmonic effects that lower the apparent Zn-(Fe,Zn) coordination number, and has observed that the Zn-(Fe, Zn) coordination number in Zn-substituted ferrihydrite decreased with increasing ratio of Zn to Zn + Fe between $0.006 < Zn/(Zn + Fe) < 0.1$. The minimum near 0.1 was attributed to a wide range of local geometries that average out EXAFS amplitudes (Waychunas et al., 2002). Thus, there is good evidence to indicate that the magnitude of Zn-Fe second neighbor interactions might be dampened within small particles that have a high Zn/Fe molar ratio.

It is also possible that Zn^{II} could become incorporated into an acid-insoluble solid phase where a lighter element, such as sulfur or phosphorus, provides a second nearest neighbor. Synthesis of Zn^{II} phosphonate crystals and Zn^{II} thiol compounds is widely reported in the literature, and Zn^{II} in these structures tend to have longer Zn-O bond lengths than for Zn^{II} sorbed to crystalline iron oxide minerals and are generally coordinated to six oxygen atoms in the reported structures (e.g., Peariso et al., 1998; Zhang et al., 1998; Song et al., 2001; Doble et al., 2002; Mao et al., 2002). Gram-negative microbial membranes contain a number of phospholipids and dynamic membrane vesicles of varying composition (Beveridge, 1999), and these organisms can respond to different nutrient conditions via the production of exopolysaccharides. Thus, differences in growth conditions could lead to associated differences in the ability for microorganisms to induce binding of Zn^{II} to cellular material. However, we took great care to perform all experiments with *S. putrefaciens* 200 cultures under nearly identical conditions and observed no indications of variability in cell viability or growth rate. Furthermore, since we did not observe large differences in the rate of Fe^{II} production in these systems, we contend that microbially enhanced Zn^{II} incorporation within goethite provides a more reasonable explanation.

5. CONCLUSIONS

These experiments indicate that sediment mineral composition places an important control on how microbial iron reduction affects sediment geochemistry, even when it has a minimal effect on the degree of "microbial reducibility." We describe two ways in which sediment mineral composition can impact the geochemical outcome of microbial iron reduction: (1) the presence of nonreducible minerals can mitigate the effect of Fe^{III} reduction on divalent metal speciation, and (2) microbial ferrihydrite reduction can incorporate previously adsorbed divalent metals into the crystal structure of an 0.5 M HCl insoluble phase that is probably authigenic goethite. The presence of nonreducible clay minerals greatly mitigates the effect(s) of microbial ferrihydrite reduction on Zn^{II} speciation, and this mitigating effect correlates with the formation of tetrahedral $ZnCl_2$ complexes that may be associated with clay mineral surfaces. These conclusions are supported by the combination of wet-chemical analyses, Mössbauer spectroscopy, and Zn *k*-edge XAS spectroscopy, and indicate that metal mobility predictions based on microbial Fe^{III} reduction experiments with synthetic iron oxide minerals may not be applicable to natural sediments that contain clay minerals.

Acknowledgments—We gratefully acknowledge the United States Department of Energy (DOE) program in Natural and Accelerated Bioremediation (DOE grant DE-FG02-97ER62482) for funding this research and for Financial Assistance Award Number DE-FC09-96SR18546 to the University of Georgia Research Foundation and Savannah River Ecology Laboratory. We also thank US DOE's Environmental Systems Research Program under contract DE-AC-07-99ID13727 BBWI for providing additional support. The Mössbauer spectroscopy was performed at the W. R. Wiley Environmental Molecular Sciences Laboratory (EMSL), a national scientific user facility sponsored by the US Department of Energy's Office of Biologic and Environmental Research and located at Pacific Northwest National Laboratory (PNNL). XAS spectroscopy was performed at the PNC-CAT facilities located at the Advanced Photon Source at Argonne National Laboratory. Research at these facilities is supported by the US DOE Office of Science grant DE-FG03-97ER45628. We would also like to specifically acknowledge Dr. Dean Hesterberg (North Carolina State University, Dept. of Soil Science) and Dr. Suzanne Beauchamin (NRC Canada—CANMET) for providing XANES spectral data for ZnS, $ZnCO_3$, $ZnSO_4$, and hydrozincite; as well as for assisting with interpretation of Fe-K-Q XAS data. We also thank Jason Rivera for his tireless efforts in the laboratory; Dr. Matilde Urrutia for performing the surface area analyses; Dr. Derek Lovely for providing *Geobacter* cultures; Arnold Erickson for assisting with XRD analyses; Dr. George Redden and several anonymous reviewers for their insightful critiques; and Master Samuel Adams for his indulgence and intellectually intoxicating insights.

Associate editor: P. Maurice

REFERENCES

Amrhein C. and Suarez D. L. (1990) Procedure for determining sodium-calcium selectivity in calcareous and gypsiferous soils. *Soil Sci. Soc. Am. J.* **54** (*4*), 999–1007.

Andreeva D., Mitov I., Tabakova V., Mitrov V., and Andreev A. (1995) Influence of iron (II) on the transformation of ferihydrite into goethite in acid medium. *Mater. Chem. Phys.* **41,** 146–149.

Ankudinov A. L. and Rehr J. J. (1997) Relativistic calculations of spin-dependent x-ray-absorption spectra. *Phys. Rev. B* **56** (*4*), R1712–R1715.

Appelo C. A. J. and Potsma D. (1996) *Geochemistry, Groundwater and Pollution*. Balkema.

Benner S. G., Hansel C. M., Wielinga B. W., Barber T. M., and Fendorf S. (2002) Reductive dissolution and biomineralization of iron hydroxide under dynamic flow conditions. *Environ. Sci. Technol.* **36** (*8*), 1705–1711.

Beveridge T. J. (1999) Structures of gram-negative cell walls and their derived membrane vesicles. *J. Bacteriol.* **181** (*16*), 4725–4733.

Bousserrhine N., Gasser U. G., Jeanroy E., and Berthelin J. (1999) Bacterial and chemical reductive dissolution of Mn-, Co-, Cr- and Al-substituted goethites. *Geomicobiol. J.* **16** (*3*), 245–258.

Caccavo F. J., Lonergan D. J., Lovley D. R., Davis M., Stolz J. F., and McInerney M. J. (1994) *Geobacter sulfurreduces* sp. nov., a hydrogen- and acetate-oxidizing dissimilatory metal-reducing microorganism. *Appl. Environ. Microbiol.* **60** (*10*), 3752–3759.

Cooper D. C., Picardal F., Rivera J., and Talbot C. (2000) Zinc immobilization and magnetite formation via ferric oxide reduction by *Shewanella putrefaciens* 200. *Environ. Sci. Technol.* **34** (*1*), 100–106.

Cornell R. M. and Schwertmann U. (1992) *The Iron Oxides: Structure, Properties, Reactions, Occurrence and Uses*. Wiley-VCH.

Doble D. M. J., Blake A. J., Cooke P. A., Parsons S., and Schroder M. (2002) Aggregation of imino-phosphonate monoester complexes. *Inorg. Chim. Acta* **331,** 336–339.

Dong H. L., Kukkadapu R. K., Fredrickson J. K., Zachara J. M., Kennedy D. W., and Kostandarithes H. M. (2003) Microbial reduction of structural Fe(III) in illite and goethite. *Environ. Sci. Technol.* **37** (*7*), 1268–1276.

Farley K. J., Dzombak D. A., and Morel F. M. M. (1985) A surface precipitation model for the sorption of cations on metal-oxides. *J. Colloid Interface Sci.* **106** (*1*), 226–242.

Fendorf S., Wielinga B. W., and Hansel C. M. (2000) Chromium transformations in natural environments: The role of biological and abiological. processes in chromium(VI) reduction. *Int. Geol. Rev.* **42** (*8*), 691–701.

Fredrickson J. K., Zachara J. M., Kennedy D. W., Duff M. C., Gorby Y. A., Li S. M. W., and Krupka K. M. (2000) Reduction of U(VI) in goethite (alpha-FeOOH) suspensions by a dissimilatory metal-reducing bacterium. *Geochim. Cosmochim. Acta* **64** (*18*), 3085–3098.

Fredrickson J. K., Zachara J. M., Kukkadapu R. K., Gorby Y. A., Smith S. C., and Brown C. F. (2001) Biotransformation of Ni-substituted hydrous ferric oxide by an Fe(III)-reducing bacterium. *Environ. Sci. Technol.* **35** (*4*), 703–712.

Fredrickson J. K., Zachara J. M., Kennedy D. W., Liu C. X., Duff M. C., Hunter D. B., and Dohnalkova A. (2002) Influence of Mn oxides on the reduction of uranium(VI) by the metal-reducing bacterium *Shewanella putrefaciens*. *Geochim. Cosmochim. Acta* **66** (*18*), 3247–3262.

Gates W. P., Stucki J. W., and Kirkpatrick R. J. (1996) Structural properties of reduced Upton montmorillonite. *Phys. Chem. Min.* **23** (*8*), 535–541.

Gates W. P., Jaunet A. M., Tessier D., Cole M. A., Wilkinson H. T., and Stucki J. W. (1998) Swelling and texture of iron-bearing smectites reduced by bacteria. *Clays Clay Minerals* **46** (*5*), 487–497.

Gerth J. (1990) Unit-cell dimensions of pure and trace metal–associated goethites. *Geochim. Cosmochim. Acta* **54** (*2*), 363–371.

Greaves G. N., Aletru C., Sankar G., Catlow C. R. A., Kempson V., and Colyer L. (1999) In situ characterisation of semiconducting nanoparticles in zeolites with XRD, XAFS and SAXS. *Jpn. J. Appl. Phys. Pt. 1* **38,** 202–205.

Hansel C. M., Benner S. G., Neiss J., Dohnalkova A., Kukkadapu R. K., and Fendorf S. (2003) Secondary mineralization pathways induced by dissimilatory iron reduction of ferrihydrite under advective flow. *Geochim. Cosmochim. Acta* **67** (*16*), 2977–2992.

Konhauser K. O. (1998) Diversity of bacterial iron mineralization. *Earth-Sci. Rev.* **43** (3–4), 91–121.

Kostka J. E. and Luther G. W. (1994) Partitioning and speciation of solid phase iron in saltmarsh sediments. *Geochim. Cosmochim. Acta* **58** (*7*), 1701–1710.

Kostka J. E., Wu J., Nealson K. H., and Stucki J. W. (1999) The impact of structural Fe(III) reduction by bacteria on the surface chemistry of smectite clay minerals. *Geochim. Cosmochim. Acta* **63** (*22*), 3705–3713.

Kostka J. E., Dalton D. D., Skelton H., Dollhopf S., and Stucki J. W. (2002) Growth of iron(III)-reducing bacteria on clay minerals as the

sole electron acceptor and comparison of growth yields on a variety of oxidized iron forms. *Appl. Environ. Microbiol.* **68** (*12*), 6256–6262.

Kukkadapu R. K., Zachara J. M., Smith S. C., Fredrickson J. K., and Liu C. X. (2001) Dissimilatory bacterial reduction of Al-substituted goethite in subsurface sediments. *Geochim. Cosmochim. Acta* **65** (*17*), 2913–2924.

Lee E. Y., Cho K. S., and Ryu H. W. (2002) Microbial refinement of kaolin by iron-reducing bacteria. *Appl. Clay Sci.* **22** (1–2), 47–53.

Liu C. X., Kota S., Zachara J. M., Fredrickson J. K., and Brinkman C. K. (2001) Kinetic analysis of the bacterial reduction of goethite. *Environ. Sci. Technol.* **35** (*12*), 2482–2490.

Lloyd J. R., Chesnes J., Glasauer S., Bunker D. J., Livens F. R., and Lovley D. R. (2002) Reduction of actinides and fission products by Fe(III)-reducing bacteria. *Geomicrobiol. J.* **19** (*1*), 103–120.

Lovley D. R. (1987) Organic matter mineralization with the reduction of ferric iron: A review. *Geomicrobiol. J.* **5** (*3/4*), 375–398.

Lovley D. R. (1991) Dissimilatory Fe(III) and Mn(IV) reduction. *Microbiol. Rev.* **55** (*2*), 259–287.

Lovley D. R. (1993) Dissimilatory metal reduction. *Annu. Rev. Microbiol.* **47,** 263–290.

Lovley D. R. (1997) Microbial Fe(III) reduction in subsurface environments. *FEMS Microbiol. Rev.* **20** (3–4), 305–313.

Manceau A., Lanson B., and Drits V. A. (2002) Structure of heavy metal sorbed birnessite. Part III: Results from powder and polarized extended X-ray absorption fine structure spectroscopy. *Geochim. Cosmochim. Acta* **66** (*15*), 2639–2663.

Mao J. G., Wang Z. K., and Clearfield A. (2002) Synthesis, characterization and crystal structures of two divalent metal diphosphonates with a layered and a 3D network structure. *Inorg. Chem.* **41** (*9*), 2334–2340.

Mehra O. P. and Jackson M. L. (1960) Iron oxide removal from soils and clays by a dithionite-citrate system buffered with sodium bicarbonate. *Clays Clay Minerals* **7,** 317–327.

Menceau F., Sankar G., Morgante N., Cristol S., Catlow C. R. A., Thomas J. M., and Greaves G. N. (2003) Characterization of zinc oxide nanoparticles encapsulated into zeolite-Y: An in-situ combined X-ray diffraction, XAFS and SAXS study. *Nucl. Instruments Methods Phys. Res. B* **199,** 499–503.

Mørup S. (1990) Mossbauer-effect in small particles. *Hyperfine Interactions* **60** (1–4), 959–974.

Murad E. (1988) Properties and behavior of iron oxides as determined by Mössbauer spectroscopy. In *Iron in Soils and Clay Minerals* (ed. J. W. Stucki and U. Schwertmann). Reidel Publishing Co..

Newville M. (2001) IFEFFIT: Interactive XAFS analysis and FEFF fitting. *J. Synchrotron Radiat.* **8,** 322–324.

Newville M., Livins P., Yacoby Y., Rehr J. J., and Stern E. A. (1993) Near-edge X-ray-absorption fine-structure of Pb—A comparison of theory and experiment. *Phys. Rev. B* **47** (*21*), 14126–14131.

Obuekwe C. O. (1980) Microbial corrosion of a crude oil pipeline. Ph.D. thesis. University of Alberta.

Pearlso K., Goulding C. W., Huang S., Matthews R. G., and Penner-Hahn J. E. (1998) Characterization of the zinc binding site in methionine synthase enzymes of *Escherichia coli*: The role of zinc in the methylation of homocysteine. *J. Am. Chem. Soc.* **120** (*33*), 8410–8416.

Picardal F. W., Arnold R. G., Couch H., Little A. M., and Smith M. E. (1993) Involvement of cytochromes in the anaerobic biotransformation of tetrachloromethane by *Shewanella putrefaciens* 200. *Appl. Environ. Microbiol.* **59** (*11*), 3763–3770.

Rancourt D. G. and Ping J. Y. (1991) Voigt-based methods for arbitrary-shape static hyperfine parameter distributions in Mossbauer-spectroscopy. *Nucl. Instruments Methods Phys. Res. B* **58** (*1*), 85–97.

Roden E. E. and Zachara J. M. (1996) Microbial reduction of crystalline iron(III) oxides: Influence of oxide surface area and potential for cell growth. *Environ. Sci. Technol.* **30** (*5*), 1618–1628.

Roden E. E. and Urrutia M. M. (2002) Influence of biogenic Fe(II) on bacterial crystalline Fe(III) oxide reduction. *Geomicrobiol. J.* **19** (*2*), 209–251.

Rosso K. M., Zachara J. M., Fredrickson J. K., Gorby Y. A., and Smith S. C. (2003) Nonlocal bacterial electron transfer to hematite surfaces. *Geochim. Cosmochim. Acta* **67** (*5*), 1081–1087.

Royer R. A., Burgos W. D., Fisher A. S., Unz R. F., and Dempsey B. A. (2002) Enhancement of biological reduction of hematite by electron shuttling and Fe(II) complexation. *Environ. Sci. Technol.* **36** (*9*), 1939–1946.

Schlegel M. L., Manceau A., Charlet L., Chateigner D., and Hazemann J. L. (2001) Sorption of metal ions on clay minerals. III. Nucleation and epitaxial growth of Zn phyllosilicate on the edges of hectorite. *Geochim. Cosmochim. Acta* **65** (*22*), 4155–4170.

Schwertmann U. and Cornell R. M. (1991) *Iron Oxides in the Laboratory: Preparation and Characterization*. VCH.

Semple K. M. and Westlake D. W. S. (1987) Characterization of iron-reducing alteromonas-putrefaciens strains from oil-field fluids. *Can. J. Microbiol.* **33** (*5*), 366–371.

Song H. H., Zheng L. M., Wang Z. M., Yan C. H., and Xin X. Q. (2001) Zinc diphosphonates templated by organic amines: Syntheses and characterizations of $NH3(CH2)_2NH_3$ $Zn(hedpH_2)_2 \cdot 2H_2O$ and $NH_3(CH_2)(n)NH_3$ Zn-2$(hedpH)_2 \cdot 2H_2O$ (n = 4, 5, 6) (hedp = 1-hydroxyethylidenediphosphonate). *Inorg. Chem.* **40** (*19*), 5024–5029.

Stookey L. L. (1970) Ferrozine—A new spectrophotometric reagent for iron. *Anal. Chem.* **42** (*7*), 779–781.

Strawn D. G. and Sparks D. L. (1999) The use of XAFS to distinguish between inner- and outer-sphere lead adsorption complexes on montmorillonite. *J. Colloid Interface Sci.* **216** (*2*), 257–269.

Stumm W. and Morgan J. J. (1981) *Aquatic Chemistry*. Wiley.

Towle S. N., Bargar J. R., Brown G. E., and Parks G. A. (1997) Surface precipitation of Co(II)(aq) on Al_2O_3. *J. Colloid Interface Sci.* **187** (*1*), 62–82.

Trivedi P., Axe L., and Tyson T. A. (2001) An analysis of zinc sorption to amorphous versus crystalline iron oxides using XAS. *J. Colloid Interface Sci.* **244** (*2*), 230–238.

Urrutia M. M., Roden E. E., Fredrickson J. K., and Zachara J. M. (1998) Microbial and surface chemistry controls on reduction of synthetic Fe(III) oxide minerals by the dissimilatory iron-reducing bacterium *Shewanella alga*. *Geomicrobiol. J.* **15** (*4*), 269–291.

Waychunas G., Davis J., and Reitmeyer R. (1999) GIXAFS study of Fe^{3+} sorption and precipitation on natural quartz surfaces. *J. Synchrotron Radiat.* **6,** 615–617.

Waychunas G. A., Fuller C. C., and Davis J. A. (2002) Surface complexation and precipitate geometry for aqueous Zn(II) sorption on ferrihydrite I: X-ray absorption extended fine structure spectroscopy analysis. *Geochim. Cosmochim. Acta* **66** (*7*), 1119–1137.

Waychunas G. A., Fuller C. C., Davis J. A., and Rehr J. J. (2003) Surface complexation and precipitate geometry for aqueous Zn(II) sorption on ferrihydrite: II. XANES analysis and simulation. *Geochim. Cosmochim. Acta* **67** (*5*), 1031–1043.

Wielinga B., Bostick B., Hansel C. M., Rosenzweig R. F., and Fendorf S. (2000) Inhibition of bacterially promoted uranium reduction: Ferric (hydr)oxides as competitive eletron acceptors. *Environ. Sci. Technol.* **34** (*11*), 2190–2195.

Zabinsky S. I., Rehr J. J., Ankudinov A., Albers R. C., and Eller M. J. (1995) Multiple-scattering calculations of X-ray-absorption spectra. *Phys. Rev. B* **52** (*4*), 2995–3009.

Zachara J. M., Fredrickson J. K., Li S. M., Kennedy D. W., Smith S. C., and Gassman P. L. (1998) Bacterial reduction of crystalline Fe^{3+} oxides in single phase suspensions and subsurface materials. *Am. Mineral.* **83** (11–12), 1426–1443.

Zachara J. M., Smith S. C., and Fredrickson J. K. (2000) The effect of biogenic Fe(II) on the stability and sorption of Co(II)EDTA(2-) to goethite and subsurface sediment. *Geochim. Cosmochim. Acta* **64** (*8*), 1345–1362.

Zachara J. M., Fredrickson J. K., Smith S. C., and Gassman P. L. (2001) Solubilization of Fe(III) oxide-bound trace metals by a dissimilatory Fe(III) reducing bacterium. *Geochim. Cosmochim. Acta* **65** (*1*), 75–93.

Zachara J. M., Kukkadapu R. K., Fredrickson J. K., Gorby Y. A., and Smith S. C. (2002) Biomineralization of poorly crystalline Fe(III) oxides by dissimilatory metal reducing bacteria (DMRB). *Geomicrobiol. J.* **19** (*2*), 179–207.

Zhang B. L., Poojary D. M., and Clearfield A. (1998) Synthesis and characterization of layered zinc biphenylylenebis(phosphonate) and three mixed-component arylenebis(phosphonate)/phosphates. *Inorg. Chem.* **37** (*8*), 1844–1852.